REPORT DOCUMENTATION PAGE

Form Approved
OMB No. 0704-0188

1. REPORT DATE *(DD-MM-YYYY)*	**2. REPORT TYPE**	**3. DATES COVERED** *(From - To)*
June 2013	Technical Paper	June 2013-July 2013

4. TITLE AND SUBTITLE
Mode Transitions in Hall Effect Thrusters

5a. CONTRACT NUMBER
In-House

5b. GRANT NUMBER

5c. PROGRAM ELEMENT NUMBER

6. AUTHOR(S)
Sekerak, M. J., Longmier, B. W., Gallimore, A. D., Brown, D. L., Hofer, R. R., Polk, J. E.

5d. PROJECT NUMBER

5e. TASK NUMBER

5f. WORK UNIT NUMBER
Q09X

7. PERFORMING ORGANIZATION NAME(S) AND ADDRESS(ES)

Air Force Research Laboratory (AFMC)
AFRL/RQRS
1 Ara Drive.
Edwards AFB CA 93524-7013

8. PERFORMING ORGANIZATION REPORT NO.

9. SPONSORING / MONITORING AGENCY NAME(S) AND ADDRESS(ES)
Air Force Research Laboratory (AFMC)
AFRL/RQR
5 Pollux Drive
Edwards AFB CA 93524-7048

10. SPONSOR/MONITOR'S ACRONYM(S)

11. SPONSOR/MONITOR'S REPORT NUMBER(S)
AFRL-RQ-ED-TP-2013-150

12. DISTRIBUTION / AVAILABILITY STATEMENT
Distribution A: Approved for Public Release; Distribution Unlimited. PA#13360

13. SUPPLEMENTARY NOTES
Conference paper for the 49th AIAA Joint Propulsion Conference, San Jose, CA, 14-17 July 2013.

14. ABSTRACT

Mode transitions have been commonly observed in Hall Effect Thruster (HET) operation where a small change in a thruster operating parameter such as discharge voltage, magnetic field or mass flow rate causes the thruster discharge current mean and oscillation amplitude to increase significantly. Mode transitions in a 6-kW class HET called the H6 were induced by varying the magnetic field intensity while holding all other operating parameters constant and measurements were acquired with ion saturation probes and ultra-fast imaging. A technique was developed that calculated discharge current density oscillations from high-speed images of the discharge channel in order to quantify the fluctuations. Two operating modes are identified as global oscillation mode and local oscillation mode. In global mode the entire discharge channel is oscillating in unison and azimuthal perturbations (spokes) are either absent or negligible. Downstream azimuthally spaced probes show no signal delay between each other and are very well correlated to the discharge current signal in global mode; in local mode they exhibit a clear signal delay between each other indicating the passage of spokes and are not well correlated to the discharge current. Spokes are localized oscillations propagating in the E×B direction that are typically 10-20% of the mean discharge current density value while the global oscillation mode can be 100% of the mean value. The transition between global mode and local mode occurred at higher relative magnetic field strengths for higher mass flow rate or higher discharge voltage. The thrust was constant through mode transition but the thrust to power decreases by 25% due in increasing discharge current. The plume showed significant differences between modes with the global mode significantly brighter in the channel and the near-field plasma plume as well as exhibiting a plasma spike on thruster centerline.

15. SUBJECT TERMS

16. SECURITY CLASSIFICATION OF:			**17. LIMITATION OF ABSTRACT**	**18. NUMBER OF PAGES**	**19a. NAME OF RESPONSIBLE PERSON**
					Daniel Brown
a. REPORT	**b. ABSTRACT**	**c. THIS PAGE**	SAR	48	**19b. TELEPHONE NO** *(include area code)*
Unclassified	**Unclassified**	**Unclassified**			661-525-5028

Mode Transitions in Hall Effect Thrusters

Michael J. Sekerak[1], Benjamin W. Longmier[2] and Alec D. Gallimore[3]
University of Michigan, Ann Arbor, MI, 48109

Daniel L. Brown[4]
U.S. Air Force Research Laboratory, Edwards Air Force Base, California 93524

and

Richard R. Hofer[5] and James E. Polk[6]
Jet Propulsion Laboratory, California Institute of Technology, Pasadena, CA 91109

Mode transitions have been commonly observed in Hall Effect Thruster (HET) operation where a small change in a thruster operating parameter such as discharge voltage, magnetic field or mass flow rate causes the thruster discharge current mean and oscillation amplitude to increase significantly. Mode transitions in a 6-kW class HET called the H6 were induced by varying the magnetic field intensity while holding all other operating parameters constant and measurements were acquired with ion saturation probes and ultra-fast imaging. A technique was developed that calculated discharge current density oscillations from high-speed images of the discharge channel in order to quantify the fluctuations. Two operating modes are identified as global oscillation mode and local oscillation mode. In global mode the entire discharge channel is oscillating in unison and azimuthal perturbations (spokes) are either absent or negligible. Downstream azimuthally spaced probes show no signal delay between each other and are very well correlated to the discharge current signal in global mode; in local mode they exhibit a clear signal delay between each other indicating the passage of spokes and are not well correlated to the discharge current. Spokes are localized oscillations propagating in the E×B direction that are typically 10-20% of the mean discharge current density value while the global oscillation mode can be 100% of the mean value. The transition between global mode and local mode occurred at higher relative magnetic field strengths for higher mass flow rate or higher discharge voltage. The thrust was constant through mode transition but the thrust to power decreases by 25% due in increasing discharge current. The plume showed significant differences between modes with the global mode significantly brighter in the channel and the near-field plasma plume as well as exhibiting a plasma spike on thruster centerline.

[1] Doctoral Candidate, Plasmadynamics and Electric Propulsion Laboratory, Department of Aerospace Engineering, 1919 Green Road, B107, Ann Arbor, MI 48105, msekerak@umich.edu, Member AIAA.
[2] Assistant Professor, Plasmadynamics and Electric Propulsion Laboratory, Department of Aerospace Engineering, 1320 Beal Avenue, Ann Arbor, MI, 48109, longmier@umich.edu, Member AIAA.
[3] Laboratory Director, Plasmadynamics and Electric Propulsion Laboratory, Professor, Department of Aerospace Engineering, College of Engineering Associate Dean for Research and Graduate, 1320 Beal Avenue, Ann Arbor, MI, 48109, alec.gallimore@umich.edu, Fellow AIAA.
[4] Research Scientist, Aerospace Systems Directorate, In-Space Propulsion Branch, Air Force Research Laboratory, 1 Ara Rd, Edwards AFB, CA, daniel.brown@edwards.af.mil, Member AIAA.
[5] Senior Engineer, Electric Propulsion Group, 4800 Oak Grove Dr., MS 125-109, Pasadena, CA, 91109, richard.r.hofer@jpl.nasa.gov, Associate Fellow AIAA.
[6] Principal Engineer; Propulsion and Materials Engineering Section, 4800 Oak Grove Dr., MS 125-109, Pasadena, CA, 91109, james.e.polk@jpl.nasa.gov, Fellow AIAA.

Nomenclature

A_b = area of discharge channel bin, cm^2
A_{chnl} = area of discharge channel, cm^2
$a(b,t)$ = average pixel value per bin
B_r = peak radial magnetic field, G
B_r^* = nominal peak radial magnetic field, G
b = bin number
c_1 = linear fit coefficient (m_0 to I_D)
c_2 = linear fit coefficient (m_0 to I_D)
e = elementary charge, 1.60×10^{-19}, C
f = frequency, s^{-1}
I_B = magnet coil current, A
$I_D(t)$ = discharge current, A
$\bar{I}_D$ = mean discharge current, A
$\hat{I}_D(t)$ = normalized, AC-coupled discharge current
$I_{D_{AC}}(t)$ = AC-coupled discharge current, A
I_{IM} = inner magnet coil current, A
I_{OM} = outer magnet coil current, A
$J_{D_b}(f,\gamma)$ = 2-D discrete Fourier transform of j_{D_b}
$j_D(t)$ = discharge current density, mA cm^{-2}
$j_{D_b}(t)$ = discharge current density per bin, mA cm^{-2}
$\bar{j}_D$ = average discharge current density, mA cm^{-2}
k_b = Boltzmann's constant, 1.38×10^{-23}, J K^{-1}
M_b = number of pixels per bin
m = spoke order
m_0 = spoke order $m = 0$
m_e = electron mass, 9.11×10^{-31} kg
m_i = Xe ion mass, 2.18×10^{-25}, kg
$\dot{m}_a$ = anode mass flow rate, mg s^{-1}
$\dot{m}_c$ = cathode mass flow rate, mg s^{-1}
N_f = number of frames
N_b = number of bins
PSD_{1D} = 1-D power spectral density, Arb Hz^{-1}
PSD_{2D} = 2-D power spectral density, Arb Hz^{-1}
$p(x,y,t)$ = pixel value
$\tilde{p}(x,y,t)$ = AC coupled pixel value
$\bar{p}(x,y)$ = mean pixel value
R_{xy} = cross-correlation between signals x and y
r_o = outer channel radius, cm
r_i = inner channel radius, cm
S_N = periodogram spectral estimate, Arb Hz^{-1}
T_e = electron temperature
$T_{e\|}$ = electron temperature parallel to magnetic field, eV
$T_{e\perp}$ = electron temperature perpendicular to magnetic field, eV
V_D = discharge voltage, V
V_f = floating potential, V
V_p = plasma potential, V
$X(f)$ = discrete Fourier transform of $x(t)$
γ = inverse angle from 2D DFT, deg^{-1}
$\bar{\varepsilon}$ = mean electron energy, eV
ε^* = material dependent cross-over energy, eV
ρ_{xy} = linear correlation coefficient between signals x and y
$\bar{\sigma}$ = effective total secondary electron emission yield
$\sigma_a(b,t)$ = uncertainty in a for bin b
$\sigma_{j_{D_b}}(b,t)$ = uncertainty in discharge current density for bin b, mA cm^{-2}
$\Delta\Phi_s$ = plasma sheath potential, V

I. Introduction

Hall Effect Thrusters (HETs) have been under development since the 1960's, first flew in the 1970's [1] and are increasingly used for and considered for a variety of space missions ranging from satellite station-keeping to interplanetary exploration. However, the physics of HET operation is not fully understood as illustrated by inconsistencies in anomalous electron transport experiment and theory, whereby an unexplained excess of electrons cross magnetic fields lines above that predicted by classical diffusion [2] or Bohm diffusion [3]. Understanding the underlying physics of HET operation is important for many reasons including the ability to create first-principle predictive models. These models would enable rapid design iterations not possible currently and would reduce

developmental costs because all existing simulations to calculate thruster performance are non-predictive and require empirical factors to match results from real thrusters. Additionally, labor and capital intensive life testing and flight qualification programs could be reduced or augmented with accurate, predictive physics based simulations. Fully understanding HET physics would ensure that ground testing adequately prepares or predicts thruster operation on orbit where the ambient pressures and local gas density on orbit are orders of magnitude lower than in ground vacuum chambers. Finally, they would facilitate scaling of HETs to very high power and or multi-channel Nested Hall Thrusters and ensure that new designs for the recently developed magnetically shielded [4] or low/zero-erosion concepts are stable across a broad operating range.

Although electron transport is not well understood in HETs, it has been noted to change significantly between different operating modes which are characterized by different thruster performance at similar operating conditions. Plasma oscillations play an integral part of mode transitions so investigating how the plasma oscillations change during mode transitions will provide insight into anomalous electron transport. Thruster performance and stability are linked to understanding plasma oscillations and the different operating modes. However, what is meant by different operating modes of an HET have not previously been described in terms of plasma oscillations within the discharge channel as will be shown in this work. This investigation induces mode transitions by varying magnetic field strength in a well characterized 6-kW class HET called the H6 and investigates oscillations with probes and high-speed imaging.

II. Modes and Transitions

HETs have been under development for over 50 years in Russia with significant experimental and flight histories [1] and mode transitions have been commonly observed throughout their development [5]. HETs have several parameters that define a single operating point such as discharge voltage, magnetic field strength (or magnet coil current), anode mass flow rate and cathode mass flow rate. HET discharge power supplies operate in voltage regulated mode where the discharge voltage between the anode and cathode is held constant and the discharge current is allowed to fluctuate. Previous research discussed below lends itself to a vague and qualitative general description of mode transition as the point while varying one parameter and maintaining all others constant, a sharp discontinuity is observed in the discharge current mean and oscillation amplitude. In one mode, the discharge current oscillation amplitude is small with respect to the mean discharge current value, while after the mode transition the mean discharge current rises sharply as well as the oscillation amplitude. Two competing ideas may play a role in mode transitions. The first idea involves wall effects and has been proposed with accompanying physical mechanism and modeling. The second idea involves more recent investigations that suggest the plume physics in the region immediately downstream from the discharge channel exit (near-field plume) may effect mode transitions, although no physical mechanism is proposed. While the answer is likely a combination of the two ideas with other outside ideas not yet proposed, investigating the plasma oscillations during mode transition may offer insight into the underlying mechanisms. This investigation only considers magnetic layer thrusters with deep discharge channels and non-conducting walls, but anode layer thrusters have exhibited similar mode transitions [6] described below.

A. Mode Transition in the SPT-100 due to Wall Effects and Space Charge Saturation

Gascon [7] investigated different wall material effects on SPT-100 thruster operation including borosil (BN-SiO_2), alumina (Al_2O_3), silicon carbide (SiC) and graphite (C). The significant differences being ion bombardment sputter yield and secondary electron emission yield coefficients as well as conductivity in the case of graphite. Here we only discuss the borosil results as the closest to the pure Boron Nitride (BN) used in the H6. Varying the magnetic field by changing the magnetic coil current (I_B) as shown in Figure 1 shows a sharp mode transition between 3.5 and 4.0 A. Below the magnetic field transition threshold the mean discharge (I_D) current and discharge current oscillation amplitudes increase significantly.

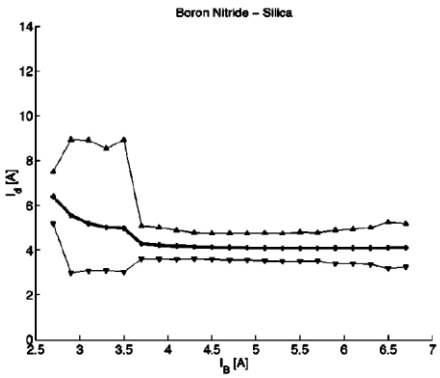

Figure 1 SPT-100 mean discharge current (crosses) and oscillation extrema (triangles) for anode flow rate of 5 mg/s and 300 V dishcarge voltage with variable magnetic field strengh represented by magnetic coil current, I_B. Reproduced from Figure 2 of [7] for borasil.

In a companion paper to Gascon's work, Barral [8] expanded on the ideas of Baitin [9] and Jolivet and Roussel [10] who considered secondary electron emission in sheath potentials of HETs. A 1-D axial fluid model was developed that accounts for electron temperature anisotropy with different electron temperatures along ($T_{e\|}$) and perpendicular ($T_{e\perp}$) to magnetic field lines. The sheath potential, $\Delta\Phi_S$, from balancing ion and electron flux to the wall with effective total secondary electron emission yield, $\bar{\sigma}$, is

$$\Delta\Phi_S = \frac{k_B T_{e\|}}{e} \ln\left[\left(1-\bar{\sigma}\right)\sqrt{\frac{m_i}{2\pi m_e}}\right] \tag{1}$$

where m_i is the ion mass, m_e is the electron mass, e is the elementary charge and k_b is Boltzmann's constant. Once $\bar{\sigma}$ approaches unity equation (1) results in a singularity and the sheath becomes space charge saturated (SCS) where the potential is no longer monotonically changing. This results in a potential well that traps electrons near the wall as shown in Figure 2. The mean energy of electrons at the wall ($\bar{\varepsilon}$), which is a function of $T_{e\|}$ and $T_{e\perp}$, determines $\bar{\sigma}$ and is a linear fit to experimental data.

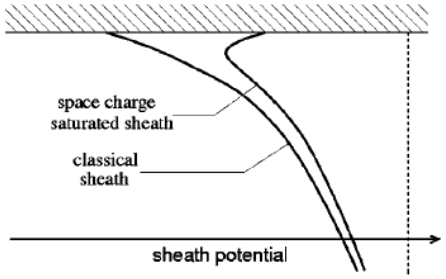

Figure 2 Sheath potential profiles at the wall with and without SCS. Reproduced from Figure 3 of [8].

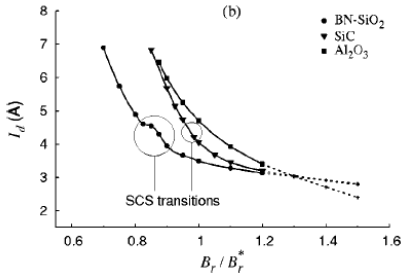

Figure 3 Simulated discharge current from 1-D fluid model with magnetic field variations for different wall materials. B_r is the maximum radial magnetic field and B_r^* is the nominal value. The steep rise in discharge current is attributed to the space charge saturation transition. Reproduced from Figure 10(b) of [8].

The classical cross-field mobility for electron transport is used in the 1-D model so no adjustable parameters to account for anomalous electron transport are used to fit experimental data [8]. Therefore the simulation results can only be qualitatively compared to experimental results. When the mean electron energy at the wall $\bar{\varepsilon}$ (which are function of $T_{e\|}$ and $T_{e\perp}$) for a given axial position in the discharge channel exceeds a material dependent cross-over energy $\left(\bar{\varepsilon} > \varepsilon^*\right)$, then $\bar{\sigma} \to 1$ and that position on the discharge channel wall is in SCS. As discharge voltage increases more energy is available to increase $T_{e\|}$ and $T_{e\perp}$ or as magnetic field is decreased energy is more easily transferred across magnetic field lines, then $\bar{\sigma}$ increases and more of the channel length is in SCS. The SCS regime starts at the maximum radial magnetic field where the electron temperature is maximum, which is at the exit plane for the SPT-100, and grows upstream in the discharge channel towards the anode.

The implication is the potential well near the wall surface for regions in SCS provides the electrons an easier path across magnetic field lines also known as near-wall conductivity. As the SCS region grows along the channel length, the low impedance path eventually reaches a region of lower magnetic field (increased mobility) or where the magnetic field lines are parallel to the wall and the electrons can easily reach the anode; resulting in a significant increase in discharge current. The magnetic field lines for the SPT-100B are shown in Figure 4 where the magnetic field lines intersect the wall perpendicularly at the exit plane in the location of maximum radial magnetic field, but the magnetic field is weaker with larger axial components parallel to the walls farther into the discharge channel. The model used in [8] is 1-D axial and only considers a radial magnetic field, while Figure 4 clearly shows the magnetic field has significant axial and radial components upstream from the exit plane. The qualitative shape of the transition between high-current to low-current is captured by the model and SCS theory as shown by comparing Figure 1 to Figure 3, however the quantitative magnitudes differ without empirical coefficients for electron transport.

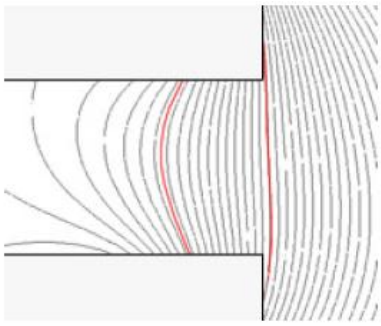

Figure 4 SPT-100B magnetic field lines. Reproduced from Figure 2a of [11].

B. Low Voltage Operation of the H6 and Azimuthal Spokes

Brown [12] showed that at low discharge voltages (100-120 V) the H6 thruster would operate either in a high-efficiency (low mean discharge current and oscillations called "low-current") or low-efficiency (high mean discharge current and oscillations or "high-current") mode with only slight differences in magnetic field settings, chamber pressure, cathode flow fractions or with externally supplied ambient gas. Figure 5 shows the discharge current decreased by approximately 10% and from Figure 13 from [12] the discharge current PSD decreased by over two orders of magnitude when transitioning from so called "high-current" mode to "low-current" mode. Note the magnetic field was varied in order to maximize efficiency for this study which may be the source of the hysteresis observed in the results. This transition occurred more readily at higher voltages (closer to flight levels) and at lower chamber pressure suggesting that the thrusters may operate differently in the space environment then test facilities on Earth. During the transition from "high-current" to "low-current" the thrust remained constant, but the increased discharge current resulted in up to a 20% decrease in thrust to power. Using an array of plume diagnostics including a nude Faraday probe, retarding potential analyzer and cylindrical Langmuir prove, Brown showed the transition from "low-current" to "high-current" corresponded to increased electron current to the anode and is therefore related to increased electron transport. Although no physical explanation is offered for the observed transitions, the effect of ambient chamber pressure, cathode flow fraction and augmented Xe flow hint at a near-field plasma plume argument involving neutral density and collision rates for mode transitions without any consideration of wall effects, which is in contrast to the ideas of Gascon and Barral [8].

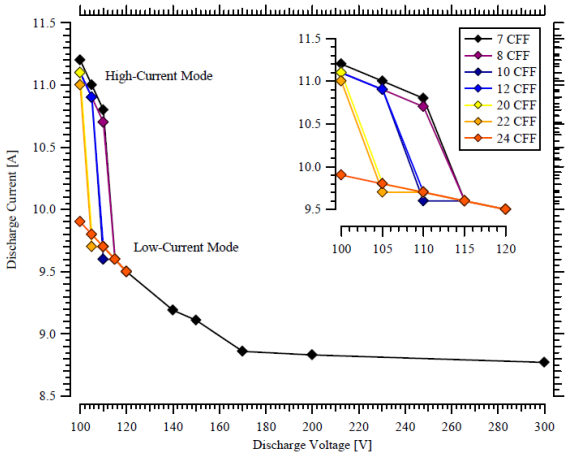

Figure 5 Change in discharge current between high-current mode and low-current mode for the H6 at low voltages. Reproduced from Figure 9 of [12]

Further research by McDonald [13] using ultra-fast imaging on the H6 in low voltage operation was the first to show the transition from "high-current" to low-current" mode correlated to stronger azimuthal oscillations or spokes. Figure 7 from [13] showed strong discharge current oscillations or strong azimuthal oscillations could be interchanged at a discharge voltage of 105 V by variation of cathode flow fraction at constant magnetic field settings. Based on the parametric study, McDonald noted that the operating mode was a stronger function of magnetic field strength than discharge voltage.

In order to understand HETs and develop first principle based models, the question of anomalous electron transport must be resolved. The transition between modes causes a change in electron current to the anode, implying that understanding mode transitions could offer insight into the unresolved question of anomalous electron transport. Furthermore, oscillations in the 10's kHz where breathing mode oscillations and azimuthal spoke oscillations are dominant are likely to play a critical role in electron transport. The previous research cited above

suggests two completely different scenarios for mode transition: 1) Plasma interaction with the wall inside the discharge channel 2) Near-field neutral or plasma properties propagating upstream into the discharge channel. The research conducted below uses time-resolved plasma diagnostics to study plasma oscillations during induced mode transitions.

III. Experimental Setup

This investigation uses the well characterized H6 HET to study mode transitions by varying magnetic field strength for various operating conditions. High-speed diagnostics including ultra-fast imaging and probes provide valuable insight into plasma oscillation changes during mode transitions.

A. H6

The H6 Hall thruster shown in Figure 6 is a 6-kW class Hall thruster with a nominal design voltage of 300 V and a 7% cathode flow fraction. It uses a hallow cathode with a lanthanum hexaboride (LaB_6) insert that can either be mounted centrally (on thruster centerline which is the nominal configuration) or mounted externally. The inner magnet coil is continuously wound while the outer coil consists of eight discrete solenoid cores wound in series and separated by 45 degrees. The outer pole is designed such that inside the discharge channel the magnetic field shown in Figure 6(Right) is azimuthally uniform to less than one Gauss. Note that the magnetic field within the discharge channel cross-section is radially symmetric about discharge channel centerline from the anode to the exit plane, whereas the SPT-100 magnetic field shown in Figure 4 is not. The H6 was a joint development effort of the University of Michigan, NASA Jet Propulsion Laboratory (JPL) and the Air Force Research Laboratory (AFRL) at Edwards AFB, and a separate copy of the thruster is maintained at each institution. It is notable for its high total efficiency, 64% at nominal 300 V, 20 mg/s (6.1 kW) operation and 70% at 800 V, 6 kW operation [14]. Slightly different nominal operating conditions are used between institutions. At the University of Michigan work by Reid, Shastry, Huang and McDonald studied operation between 5 and 30 mg/s flow rates, but primarily focused on 20 mg/s for approximately 6 kW operation at 300 V. Work by Hofer at the JPL has tuned the H6 to even discharge currents and power levels, i.e., 20 A for exact 6 kW operation at 300 V. For xenon these operating conditions vary only by a few percent in current or mass flow rate (1 mg/s Xe ~ 1 A), but peak magnetic field strengths between the two cases may vary by up to 15%. At the 300 V, 20 mg/s Michigan operating condition the H6 has a 20.3 A discharge current, produces 397 mN of thrust at a specific impulse of about 1900 s [15]. At the nominal 300 V, 20 A, 6 kW JPL condition, the specific impulse is 1950 s with a thrust of 401 mN [14].

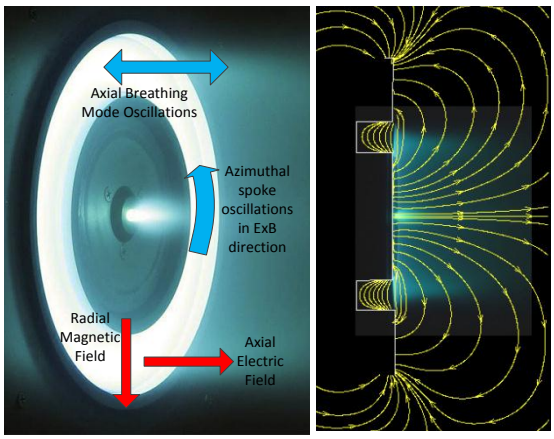

Figure 6 (Left) H6 with direction of magnetic field and E×B shown. (Right) Profile picture of the H6 operating at nominal conditions with magnetic field stream lines overlaid and discharge channel outlined.

Since first firing in 2006 the H6 has been well characterized by a variety of diagnostic and modeling techniques at Michigan, JPL and AFRL. Six experimental doctoral dissertations have focused on the thruster to date, [15–20] which have spawned numerous associated conference and journal articles. Modeling of the H6 has been performed using the hybrid Particle-In-Cell (PIC) simulation HPHall-2 [21] and the more recently developed fluid code Hall-2De [22]. The H6 is a well characterized HET with multiple references for steady-state values and provides an ideal platform for high-speed investigations of oscillatory plasma phenomena undoubtedly present.

Table 1 Test matrix showing discharge voltage and anode flow rate variations for the internal cathode configuration. Green: tested, Red: not tested. Number indicates the number of sweeps at the condition.

	14.7 mg/s	19.5 mg/s	25.2 mg/s
300 V	1	4	1
400 V	0	2	0
450 V	0	1	0

Table 1 shows the test matrix where the H6 was operated with xenon propellant at voltages of 300, 400 and 450 V applied between the anode and cathode. Propellant mass flow rates tested were 25.2, 19.5 and 14.7 mg/s through the anode and 1.8, 1.4 and 1.0 mg/s (7% cathode flow fraction) through the LaB6 cathode, respectively. The flow rate of 19.5 mg/s is the nominal setting used for comparison in this work and the cathode flow fraction of 7% was maintained for all conditions. Internal or centerline mounted cathode mounting is the nominal configuration of the H6 as shown in Figure 6 and Figure 7(Top), but an external cathode configuration was also tested and shown in Figure 7(Bottom). The only data presented here for the external configuration is the nominal 300 V, 19.5 mg/. Unless explicitly stated, all data shown below is for the internal cathode configuration. The magnetic field shape shown in Figure 6(Right) was kept constant during testing, though the magnitude, noted by B_r/B_r^*, was varied throughout the testing in order to induce a mode change within the H6. The nominal magnetic field (B_r^*) strength (i.e., for maximum thruster performance) at 300 V and 20 A discharge current required an inner magnet (I_{IM}) current of 3.50 A and outer magnet (I_{OM}) current of 3.13 A [14].

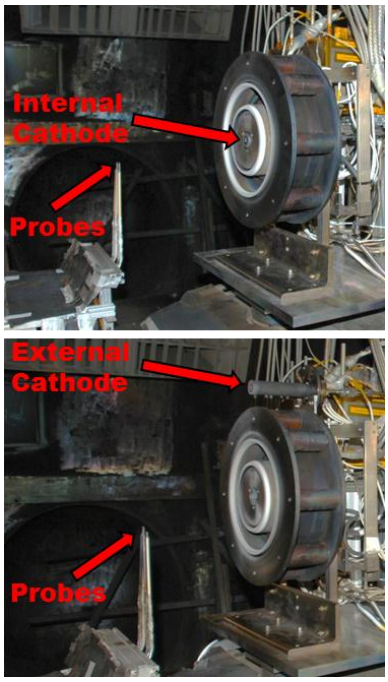

Figure 7 Internal cathode (Top) and external cathode (Bottom) configurations shown with probes.

B. Facilities and Thruster Telemtry

Testing occurred in the Large Vacuum Test Facility (LVTF) of the Plasmadynamics and Electric Propulsion Laboratory (PEPL) at the University of Michigan. The LVTF is a 200 m^3 stainless steel-clad vacuum chamber 9 m long and 6 m in diameter. Rough vacuum is achieved with two 2000 CFM blowers backed by four 400 CFM mechanical pumps with a final base pressure in the low 10^{-7} Torr achieved by seven CVI TM-1200 re-entrant cryopumps with LN_2 baffles and a nominal pumping speed of 500,000 L/s on air or 240,000 L/s on xenon. During thruster operation the chamber pressure was measured with a nude ion gage at the top of the chamber downstream from the thruster location with an uncertainty of $\pm 0.1\times10^{-6}$ Torr. Pressure varied for conditions based on anode flow rate and with a fixed chamber pumping speed. The xenon corrected pressures were 6.1×10^{-6}, 9.0×10^{-6} and 1.2×10^{-5} Torr for 14.7, 19.5 and 25.2 mg/s anode flow rate, respectively. Discharge voltage and current to the thruster was supplied with an Amrel 100 kW DC power supply across a 102 mF Maxwell Laboratories Caster Oil capacitor. Telemetry including mean discharge current, cathode to ground voltage, discharge voltage, inner and outer magnetic currents and voltages were measured at 1 s intervals with an Agilent 34970A Data Logger and recorded on a PC using Agilent Benchlink software. The discharge voltage (V_D) was measured between sense lines on the anode and cathode and input through a 10,000:1 voltage divider calibrated with the power supply and BK Precision 5491A multimeter. Mean discharge current $\bar{I}_D = \langle I_D(t) \rangle$ where $\langle\ \rangle$ denotes average was measured with an NT-50 FW Bell sensor and magnet coil currents were measured across 10 mΩ shunt resistors. All currents were calibrated using a precision 10 mΩ resistor accurate to 0.1% and a BK Precision 5491A multimeter. The plume photographs were taken with a Nikon D80 digital camera with a DX AF-S Nikkor 18-135 mm lens set to f5.6, 1/100 s shutter speed and manual focus.

The xenon propellant is delivered to the HET using Alicat Scientific MC Series mass flow controllers through electro-polished stainless steel lines. Mass flow calibration takes place through a Bios Definer 220L DryCal system plumbed in parallel to the anode and cathode feed lines with an accuracy of 1% of reading between 5-500 sccm. Mass flow calibrations are taken for each mass flow controller at several flow rates and a linear fit is used to determine the flow produced at any arbitrary set point. The AC component of the thruster discharge current, $I_{D_{AC}}(t)$

was measured either with a Tektronix TCP 312 (DC-100 MHz bandwidth) or TCP 303 (DC-15 MHz bandwidth) split-core Hall current sensors through a Tektronix TCPA 300 Current Probe Amplifier. The signal was measured on the discharge current line external to the chamber on the anode side and was acquired simultaneously with HDLP-ISR signals on the same Data Acquisition (DAQ) system described later. The total discharge current, time history signal is the combination of the two measurements

$$I_D(t) = \bar{I}_D + I_{D_{AC}}(t) \tag{2}$$

Discharge current oscillation amplitude will be defined here as the root-mean-square (RMS) of the AC-coupled discharge current time history signal $\tilde{I}_D = \sqrt{\langle I_{D_{AC}}(t)\rangle^2} = \sqrt{\langle (I_D(t) - \bar{I}_D)^2 \rangle}$ in A or the RMS value fraction of the mean discharge current $\tilde{I}_D / \bar{I}_D$. The normalized, AC-coupled discharge current, $\hat{I}_D(t)$, is calculated from the discharge current time-history signal, by

$$\hat{I}_D(t) = \frac{I_D(t) - \bar{I}_D}{\tilde{I}_D} \tag{3}$$

Discharge current density average $\bar{j}_D$ and time history $j_D(t)$ values are defined as

$$\bar{j}_D = \frac{\bar{I}_D}{A_{chnl}} \tag{4}$$

$$j_D(t) = \frac{I_D(t)}{A_{chnl}} = \frac{\bar{I}_D + I_{D_{AC}}(t)}{A_{chnl}} \tag{5}$$

where $A_{chnl} = \pi\left(r_o^2 - r_i^2\right)$ is the area of the discharge channel with outer and inner radius, r_o and r_i, respectively.

An inverted pendulum thrust stand is used in LVTF based on the NASA Glenn Research Center design of Haag [23]. This design has extensive heritage for testing electric propulsion devices [15, 18, 24] so the details will not be recapitulated here. In summary, the inverted, pendulum thrust stand operates in null mode using a Proportional, Integral, Derivative (PID) controller to maintain a vertical positions based on feedback from an Linear Variable Differential Transformer (LVDT) and a solenoid actuator. An inclinometer is used to ensure the thrust stand is level after shifting of the facility during pump down and thruster operation. A cooling loop with glycol powered by a Polyscience Durachill 6860T chiller with 5.2 kW cooling capacity is used to thermally regulate the thrust stand. The thruster was operated for over three hours before any data was acquired in order for the thruster and thrust stand to reach thermal equilibrium. While the thrust stand may not have been at complete thermal equilibrium, this is accounted for by taking zero values at regular intervals where the thruster is briefly turned off and the zero output is recorded. The thrust stand was calibrated by lowering and raising a series of calibrated weights to ensure a linear response, which was performed before thruster operation, two times during testing when the thruster was briefly turned off, and once again after testing was complete. All calibrations showed a linear response and were combined to generate the thruster calibration curve to convert PID output in V to thrust in mN.

C. Probes

A pioneering technique for time-resolved plasma property measurements has been developed by Lobbia called the High-Speed Dual Langmuir Probe (HDLP) [25] which can measure plasma properties at rates of 100's kHz [26]. The technique was recently extended by Sekerak to add an Ion Saturation Reference (ISR) probe [27] to measure ion density and augment the HDLP signal with a DC reference. Each HDLP-ISR consists of an active probe, null probe and ISR probe as shown in Figure 8. Both the active and null probes were 0.13 mm diameter pure tungsten wire with 3 mm exposed for the active HDLP probes and ISR probes; the null probe by design does not have any exposed wire.

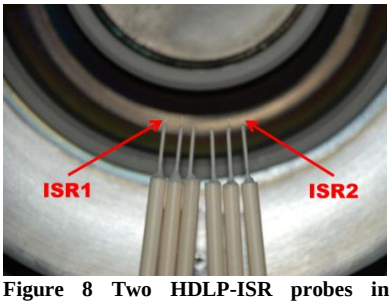

Figure 8 Two HDLP-ISR probes in position at the 6 o'clock location. A complete HDLP-ISR consists of an active probe, a null probe and an ISR probe. The exposed Tungsten wire is only near the arrow tip.

The ISR signal alone can provide useful information for identifying plasma oscillations without actually calculating plasma properties and is the only data reported here. The time resolved plasma property measurements of electron density, plasma potential and electron temperature will be reported in

a future publication. According to thin sheath Langmuir probe analysis [28, 29], I_{ISR} is linearly related to ion density at constant electron temperature if the probe is operated in ion saturation. Previous work mapped the plasma plume of the H6 with a discharge voltage of 300 V and discharge current of 20 A for the nominal magnetic field, $B_r/B_r^* = 1$ [27]. Using the plume information from Figure 14 and 15 of [27] the respective electron temperature and plasma potential are 3.7 eV and 30 V with respect to ground. In order to ensure the ISR probes are in ion saturation, they must be biased well below the floating potential, which from equation (7) of [27] is

$$V_f \approx V_p - 5.8T_e \tag{6}$$

where T_e is the time-averaged electron temperature in eV. The ISR probes were biased to -30 V with respect to ground which was more than 16 T_e below the plasma potential and are safely in ion saturation. During this investigation magnetic field, discharge voltage and flow rate are varied so the plume properties will differ from those reported in [27], but the changes are not expected to be enough such that the probes were not in ion saturation when they have a factor of 3 margin at nominal conditions.

The ISR current is measured external to LVTF across a 100 Ω shunt resistor through an Analog Devices AD 215 120 kHz low distortion isolation amplifier where the 2 μs offset has been accounted for. The 2 μs offset was specified on the data sheet and verified using the AFG3010 and a Tektronix digital oscilloscope. The data acquisition system used to record discharge current and the ISR signals are sampled at rates up to 180 MHz with 16-bit AlazarTech ATS9462 digitizers.

The probes were moved in place using a 1.5 m long Aerotech ATS62150 ball screw stage driven by a stepper motor and controlled with an Aerotech MP10 controller. It is used in open loop position feedback mode with a 15 V string potentiometer to monitor the stage position during movement and ensure proper positioning in front of the thruster to within 5 mm radially. Figure 8 shows the two HDLP-ISRs in position in front of the thruster 1.5 mean channel radii downstream in the 6 o'clock position on discharge channel centerline ±5 mm. The ISR probe gap was 29.5 ±0.5 mm apart, which is 21.4° ±1.7° azimuthal spacing (10.7° on either side of 6 o'clock).

The Pearson linear correlation coefficient or product-moment coefficient of correlation ρ_{xy} is used to quantify how well two signals, *x* and *y*, are correlated [30]

$$\rho_{xy} = \frac{\sum_N \left(x_i - \langle x \rangle\right)\left(y_i - \langle y \rangle\right)}{\sqrt{\sum_N \left(x_i - \langle x \rangle\right)^2 \sum_N \left(y_i - \langle y \rangle\right)^2}} \tag{7}$$

This technique will be used to show correlation from discharge current to ISR probe signals and between probe signals. The coefficient ranges from $-1 \le \rho_{xy} \le 1$ where 1 means the signals are perfectly correlated ($x = y$), -1 means they are inversely correclated ($x = -y$) and 0 means they are not correlated. Additionally, the cross-correlation is used extensively to calculate the time-offset between two signals. The cross-correlation function is [30]

$$R_{xy} = \lim_{T\to\infty} \frac{1}{T} \int_0^T x(t)\, y(t+\tau) dt \tag{8}$$

Signal delays for non-frequency dispersive propagation can be identified by peaks in R_{xy} as is done with discharge current to probe signals and between probe signals. When using calculating R_{xy} from equation (8) the signals are first AC-coupled and normalized and the time delay is determined from the largest peak in R_{xy}.

IV. High-speed Imaging Analysis

A pioneering high-speed image analysis technique was developed by McDonald [19, 31, 32] to investigate azimuthal oscillations from videos. Here the technique has been adapted to transform the videos into measurements of discharge current density distribution in the discharge channel in order to quantify oscillations. These techniques will be referred to as High-speed Image Analysis (HIA) throughout the following discussion.

A. Equipment and Image Enhancement

High-speed imaging was acquired with a Photron SA5 FASTCAM with a Nikon ED AF Nikkor 80-200mm lens at its maximum aperture f/2.8. The SA5 is capable of up to 1,000,000 fps with 128×16 pixel resolution, but was used at 87,500 fps with 256×256 pixel resolution for this testing. The camera was 6 m downstream from the thruster outside LVTF with a view of the thruster through a viewport. The image enhancement technique developed by McDonald [32] allows for easy visualization of rotating spokes as shown in Figure 9. When watching the raw FastCam video the rotating spokes are very clear to the casual observer; the visualization technique shown in Figure 9 is only meant to enhance what is unambiguously present. Here small fluctuations in light intensity from a mean value can be seen and have been shown to rotate in the E×B direction as azimuthally propagating spokes. It is important to note that the pixel value corresponding to light intensity is not a direct measure of plasma properties. However, if light is assumed to be produced primarily by collisional processes then the brightness can be interpreted as a proxy for collision rates and by extension density or discharge current. Also important is that the camera records an integrated light intensity through the plume to the anode, meaning it cannot distinguish where the brightest regions of the plume are located axially.

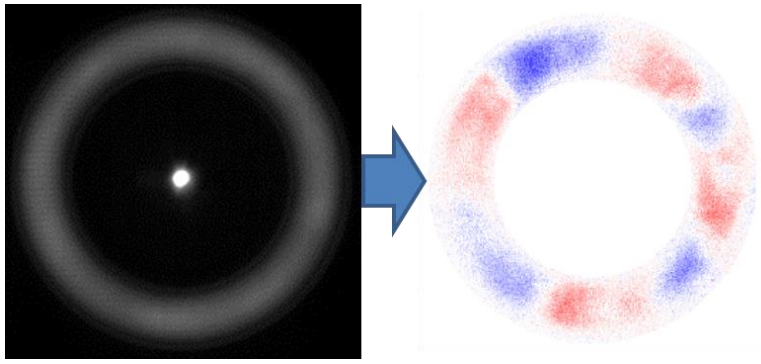

Figure 9 Raw FastCam video frame and subsequent enhancement with the McDonald technique to visualize spokes.

B. Analysis Method

The Fourier analysis techniques developed by McDonald [31] have been adapted to process the FastCam videos to determine breathing and spoke mode frequencies. The high-speed imaging technique is comprised of the following steps:

1. Import the raw video file into MatLab as a $p(x,y,t) = 256 \times 256 \times N_f$ matrix, where N_f is the number of frames in the video. The Photorn SA5 has a 12 bit sensor, so each pixel, *p*, has 2^{12} =4096 possible values assumed to linearly represent light intensity.
2. Calculate and subtract the mean image $\bar{p}(x,y)$ from each frame in order to AC couple the video $\tilde{p}(x,y,t) = p(x,y,t) - \bar{p}(x,y)$. The mean image is a 256×256 matrix where each pixel has been averaged across all N_f frames. The camera is vertically level with the thruster and offset horizontally with an angle of 2.5 degrees to the left of thruster centerline therefore it has a more direct view of the 6 to 12 o'clock region of the channel. A more direct view through the plume to one side of the discharge channel will skew the analysis because that area of the discharge channel will always be brighter since the image is integrated through the plum to the back of the anode. In this case, the 9 o'clock region is always brighter and 3 o'clock always dimmer due to the camera offset. This step of AC-coupling removes that bias.
3. Automatically identify the center of the circular discharge channel using a Taubin circle fit and isolate the annular region of the discharge channel in each frame.
4. Considering the pixels in cylindrical coordinates $\tilde{p}(x,y,t) \rightarrow \tilde{p}(r,\theta,t)$, divide the annulus into N_b= 180 two-degree bins, *b*, and determine which pixels from the 256×256 array belong to each bin. Each bin has M_b = 120 to 160 pixels.
5. Average the pixel value for each bin to generate a 180×1 vector of light intensity values for each frame.

$$a(b,t) = \frac{\sum_{r=r_i}^{r_o} \sum_{\theta=\theta_b}^{\theta_{b+1}} \tilde{p}(r,\theta,t)}{M_b} \tag{9}$$

6. Calculate the $m = 0$ or m_0 spoke order, which is the entire channel added together.

$$m_0(t) = \sum_{b=1}^{N_b} a(b,t) \tag{10}$$

7. The discharge current is linearly related to the $m_0(t)$ spoke order as will be shown later in Figure 14. Down-sampled $I_D(t)$, which has a native bandwidth above 1 MHz, to the camera frame rate of 87.5 kHz using an 8th order Chebyshev Type 1 filter to smooth and resample. Apply a linear, least squared fit to relate I_D to m_0, where c_1 and c_2 are the resulting linear coefficients. Note, the total discharge current $I_D(t)$ can be written as the sum of the discharge current through each bin, $I_{D_b}(b,t)$. Assuming the offset coefficient, c_2, can be equally distributed amongst the bins so as to be pulled into the summation. The discharge current can then be written as

$$I_D(t) = \sum_{b=1}^{N_b} I_{D_b}(b,t) = c_1 m_0(t) + c_2 = \sum_{b=1}^{N_b} \left(c_1 a(b,t) + \frac{c_2}{N_b} \right) \tag{11}$$

The local discharge current density j_{D_b} for bin b is then

$$j_{D_b}(b,t) = \frac{I_{D_b}(b,t)}{A_b} = \frac{c_1}{A_b} a(b,t) + \frac{c_2}{A_b N_b} \tag{12}$$

8. The discharge current density surface is a $180 \times N_f$ matrix for the angular discharge current density over time as shown in Figure 10 and discussed in more detail below with uncertainty analysis.
9. Perform a 2-D discrete Fourier transform (DFT) on the discharge current density surface to compute frequency and order number. The magnitude of the 2-D DFT generates a PSD surface map of frequency (1/s) versus 1/deg or 1/rad using equation (19) as discussed below. The angular location is converted to spoke order (m) which are the number of spokes present in the channel and are shown in Figure 15 and Figure 16.

The significance of equation (12) is that the local discharge current density in the channel can be calculated from high-speed images which are unitless pixel values based on light intensity. This is accomplished with non-intrusive measurements using instruments outside the vacuum chamber.

C. Uncertainty Analysis

Significant error or uncertainty can be introduced with the assumptions above, but they are easily quantified. Three primary sources of uncertainty will be considered, other sources of uncertainty such as probe resolution and calibration uncertainty are assumed to be of lower order.

1. Standard deviation of pixel values in bin b from the mean pixel value, a. This will be different for each bin b and time t.
2. Error from the linear fit of $m_0(t)$ to $I_D(t)$, which will vary in time but be applied equally for each bin b.
3. Difference between $I_D(t)$ at the native sampling rate or full bandwidth of the current probe (whichever lower) and $I_D(t)$ down-sampled to the camera frame rate. This will vary in time but also be applied equally for each bin b.

The total error in j_{D_b} is the sum of the three error sources considered above:

$$\sigma_{j_{D_b}}(b,t) = \sigma_{j_{D_b}1}(b,t) + \sigma_{j_{D_b}2}(t) + \sigma_{j_{D_b}3}(t) \tag{13}$$

The standard deviation for the pixel value in bin b is computed similar the average value calculated in equation (9).

$$\sigma_a(b,t) = \left[\frac{1}{M_b - 1} \sum_{r=r_i}^{r_o} \sum_{\theta=\theta_b}^{\theta_{b+1}} \left(\tilde{p}(r,\theta,t) - a(b,t) \right)^2 \right]^{1/2} \tag{14}$$

Using the error propagation equation [33] on equation (12) yields

$$\sigma_{j_{D_b}1}(b,t) = \frac{\partial j_{D_b}}{\partial a} \sigma_a(b,t) = \frac{c_1}{A_b} \sigma_a(b,t) \tag{15}$$

where the error in c_1 and c_2 will be accounted for in $\sigma_{j_{D_b}2}$. The standard deviation of the error in I_D calculated from the linear fit with m_0 is $\Delta I_D(t)$, which is computed during the least-squared linear fit and encompasses 50% of predictions in I_D from m_0. The uncertainty introduced by the linear fit between I_D and m_0 is

$$\sigma_{j_{D_b}2}(t) = \frac{\Delta I_D(t)}{A_{chnl}} \tag{16}$$

The discharge current I_D is filtered and down-sampled to correlate with m_0 as described in Step 7. It is then up-sampled using interpolation to calculate the difference with the native I_D. The difference is resampled at the camera frame rate without smoothing or filtering in order to determine the difference between native and down-sampled discharge current.

$$\sigma_{j_{D_b}3}(t) = \frac{\left| \left\{ I_D(t) \right\}_{Native} - \left\{ I_D(t) \right\}_{DownSampled} \right|}{A_{chnl}} \tag{17}$$

For a mean discharge current of $\bar{I}_D = 20\text{A}$ the average discharge current density is $\bar{j}_D = 133\text{mA/cm}^2$. An error of 1 A in discharge current for equation (16) or (17) yields an uncertainty of 6.6 mA/cm^2 for $\sigma_{j_{D_b}2}$ or $\sigma_{j_{D_b}3}$ while an error of 10 A yields uncertainty of 66 mA/cm^2. Regardless of the uncertainty introduced, the method outlined above provides meaningful quantification of FastCam images to discuss oscillation amplitudes during mode transitions.

An example of a discharge current density surface plot calculated from equation (12) is shown in Figure 10(a) with the uncertainty calculated from equation (13) shown in Figure 10(b). In the discharge current density surface plot, the ordinate is azimuthal location around the discharge channel in clock positions and the abscissa is time with each vertical column of values representing one frame of video. Vertical features in the discharge current density surface plot represent extremes in discharge current density that occur everywhere in the channel simultaneously. Horizontal features would be discharge current values that remain constant at a fixed azimuthal location, which is not typically observed. Diagonal features are perturbations in discharge current density that propagate azimuthally around the discharge channel. Lines from upper-left to lower-right are propagating counter-clockwise around the discharge channel and lines from the lower-left to upper-right are propagating clockwise. The E×B direction in the H6 is counter-clockwise since the B-field direction is radially out, and it will be shown later that all azimuthally propagating features are in that direction represented by lines from upper-right to lower-left with the slope corresponding to propagation velocity in deg/s. While in global mode, the discharge current rises in approximately 20-40 μs as shown in Figure 17, but the FastCam frame rate of 87,500 fps yields a resolution of 11.4 μs which introduces error while matching m_0 and I_D in equation (16).

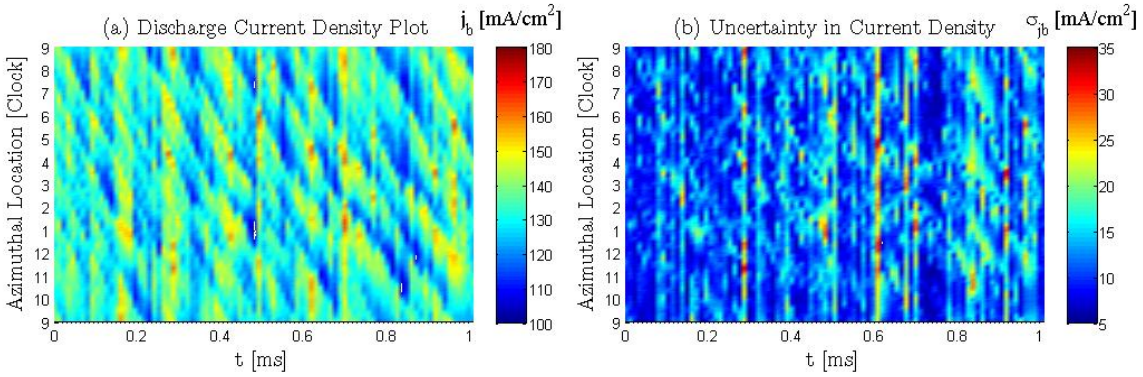

Figure 10 (a) Discharge current density plot for 300 V, 19.5 mg/s, Br/Br* = 1, (b) Uncertainty in discharge current density.

The discharge current density plots have the same features as the discharge current density surface plots developed by McDonald [31], but the scaling has physical units and they are used to investigate and visualize global discharge channel oscillations as well as azimuthally rotating spokes.

D. Power Spectral Density

Several methods can be used to describe the frequency response of a signal, so here we define the methods and formulas used below. If *X(f)* is the 1-D discrete Fourier transform (DFT) of a time-series signal *x(t)* with length N, then the periodogram spectral estimate $S_N(f)$ of the signal [34], which is an estimate of the power spectral density (PSD) without scaling [35], is

$$PSD_{1D}(f) = S_{N1D}(f) = \frac{1}{N} X^*(f) \cdot X(f) \tag{18}$$

where $X^*(f)$ is the complex conjugate. A 2-D DFT of the discharge current density surface plot $j_{D_b}(t,\theta)$ produces $J_{D_b}(f,\gamma)$ where γ is in units of 1/deg. Fourier transforms can be extended to multiple dimensions, so by analogy to equation (18) the 2-D PSD is

$$PSD_{2D}(f,\gamma) = S_{N2D} = \frac{1}{N_f N_b} J^*_{D_b}(f,\gamma) \cdot J_{D_b}(f,\gamma) \tag{19}$$

The analysis of PSDs below only compares the change in relative magnitude of the PSDs through mode transitions, so without proper scaling on equations (18) and (19) the units will be listed as Arbitrary Units/Hz in Figure 15 and Figure 16. In a 2-D Fourier transform of a surface where one axis is time and the other is angle (degrees), one axis of the transformed surface will be similar to a typical 1-D Fourier transform of a time history signal with units of f = 1/s or Hz and the other will yield γ = 1/deg. Multiplying γ by 360 deg/circle yields the spoke order m or number of segments per circle (e.g. m = 3 means three segments or three spokes). As described by McDonald in his original derivation [31], this is analogous to number of wave lengths per channel circumference. Hence m = 0 or m_0 is no wave in the channel (the entire channel is dark or bright), m = 1 means one wave in the channel (one half bright, the other dark), m = 2 is two waves per channel (two bright regions, two dark regions), m = 3 is three waves per channel (three bright regions, three dark regions), etc. Equation (18) is used to calculate the PSDs for discharge current and ISR probe current, both of which have been AC coupled to remove the large value at f = 0 when there is a DC offset. When computing the 1-D DFT for $I_{D_{AC}}$ and I_{ISR} a Blackman window is used and when computing the 2-D DFT of j_{D_b} a Hamming window is used.

V. Results

The measurement tools and data analysis techniques described above were used to intentionally induce and analyze mode transitions in the H6 by varying magnetic field magnitude. Magnetic field sweeps, or B-field sweeps denoted by B_r/B_r^*, were conducted with all other parameters including discharge voltage, flow rate and chamber pressure, held constant until the thruster transitioned modes and eventually became unstable. For reasons that will be made clear and discussed in great detail below, the B_r/B_r^* region of decreased discharge current mean and oscillation amplitude will be called local oscillation mode and the B_r/B_r^* region of increased discharge current mean and oscillation amplitude will be called global oscillation mode.

A. Transition

The magnetic field was varied by changing the inner and outer magnet coil currents in a constant ratio with all other parameters held constant including flow rates, discharge voltage, and chamber pressure. Maintaining a constant 1.12 ratio of inner to outer coil current allowed the magnetic field magnitude to be varied without changing the shape shown in Figure 6, i.e. the B-field lines were constant. The magnetization or BH curve of a material is a relation between the magnetic intensity ($\vec{H}$) and the magnetic induction or field ($\vec{B}$) which are related by the permeability (μ). The BH curve is material specific and can saturate causing distortions in the applied B-field of the HET. The H6 consists of iron pole pieces with carefully selected BH curves that begin to saturate above approximately 5.5 A of coil current, which set the upper bound of magnetic field testing at I_{IM} = 5.50, I_{OM} = 4.92 A or $B_r/B_r^* = B_r/B_r^*|_{\max} = 1.57$. Magnetic field sweeps were typically started from $B_r/B_r^*|_{\max}$ and decreased until the thruster discharge was unstable. However, a 300V sweep was conducted starting from $B_r/B_r^*|_{\max}$ decreasing until thruster instability and then increased again returning to $B_r/B_r^*|_{\max}$ in order to demonstrate directionality independence and the absence of hysteresis. The thruster was operated for approximately 3-5 minutes at each B_r/B_r^* setting during a sweep. In order to ensure thermal equilibrium, the thruster was operated for a minimum of 3 hours before conducting B-field sweeps and when changing conditions (discharge voltage or flow rates) was operated for 0.5 to 1 hours prior to sweeps. All flow rates at 300 V discharge voltage were repeated during different pump downs where the thruster was exposed to atmosphere between tests. Tests were also repeated with and without the probes shown in Figure 8 present in order to ensure the probes were not significantly altering the thruster operation.

Decreasing B_r/B_r^* below a certain threshold was shown to repeatedly induce a mode transition similar to those discussed in Section II where the mean discharge current increased and the discharge current amplitude increased. This was shown consistently for the three different voltages (300, 400 and 450 V) and three different flow rates (14.7, 19.5 and 25.2 mg/s) as shown in Figure 11 and Figure 12. The $\bar{I}_D$ and $\tilde{I}_D$ vs B_r/B_r^* shows two distinct

regions with a transition line. We define the thruster to be more sensitive to mode transitions if the transition occurs at higher B_r/B_r^* values. Because $B_r/B_r^*|_{max}$ is an upper limit due to material properties inherent with the thruster design, if the transition point occurs at higher B_r/B_r^* then the range of B-field values where the thruster operates in local mode is diminished. As will be shown later, defining a single transition value for the B-field is misleading because there is a transition region where the plasma exhibits both types of oscillations, however the transition typically occurred over only~10% change in B_r/B_r^*.

Figure 11 and Figure 12 shows that increasing discharge voltage or flow rate makes the thruster more sensitive to mode transitions. Figure 11 (a) and (b) show the discharge current mean and oscillation amplitude, respectively, for discharge voltages of 300, 400 and 450 V. The parenthetical numbers in the legend show the number of sweeps where the 300V condition was repeated three times (including one continuous decreasing then increasing sweep and one sweep with probes) and the 400 V condition was repeated twice (once with probes and once without). The different sweeps showed remarkable consistency with deviations less than 3% of the mean indicating the transitions were not caused by transient thruster properties such as out-gassing or thermal dis-equilibrium.

Figure 12 show that increasing anode flow rate with a constant 7% cathode flow fraction makes the thruster more sensitive to mode transitions. Figure 12 (a) and (b) show the discharge current mean and oscillation amplitude, respectively, for anode flow rates of 14.7, 19.5 and 25.2 mg/s. Only 1 sweep at 14.7 mg/s is shown, although a second was conducted before all current sensors were calibrated and it yielded identical results. A second sweep at 25.2 mg/s was also conducted and not shown where the thruster was not operated at that flow rate for adequate time to reach thermal equilibrium, which caused a shift in mode transition. After adequate equilibrium time, the transition region stabilized. The higher discharge voltages of 400 V and 450 V showed a steadily increasing oscillation amplitude for $B_r/B_r^* > 1$, yet the mean discharge current remained the same. The lowest flow rate case of 14.7 mg/s for 300 V showed significantly higher oscillation amplitude for $B_r/B_r^* > 1.2$ than the other flow rates indicating a possible transition to an entirely different mode than the transition between global and local mode at $B_r/B_r^* = 0.53$.

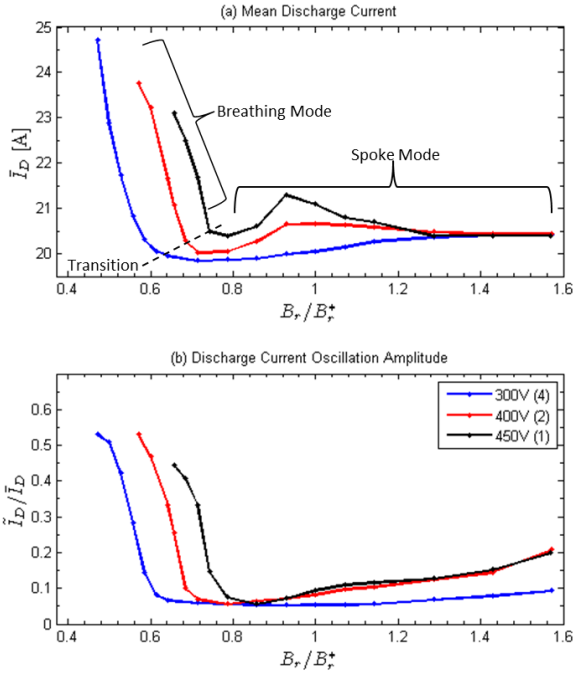

Figure 11 Discharge current mean (a) and oscillation amplitude (b) variation with constant 19.5 mg/s anode flow rate and variable discharge voltages of 300, 400 and 450 V. The number in parenthesis is the number of sweeps averaged together.

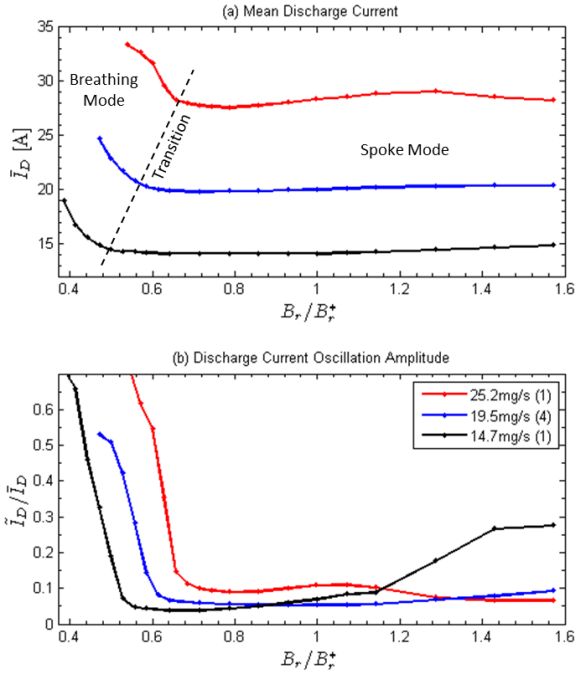

Figure 12 Discharge current mean (a) and oscillation amplitude (b) variation with constant 300 V discharge and variable anode flow rates of 25.2, 19.5 and 14.7 mg/s. The number in parenthesis is the number of sweeps averaged together.

A distinction needs to be drawn between oscillatory operation in global mode and unstable operation. An increase in discharge current mean and oscillation amplitude is often labeled as unstable operation; however the thruster shows no sign of run-away behavior. Here we define unstable operation as the condition where discharge current begins to rise uncontrollably at a constant B-field setting. Figure 13 shows a typical B-field sweep at 300 V, 19.5 mg/s, lasting less than 1 hour with approximately 3 minutes at each setting. The continuously recorded values for inner magnet current I_{IM} and mean discharge current $\bar{I}_D$ are shown Figure 13 with the discrete values used in later plots shown as symbols. Representing B_r/B_r^*, I_{IM} is decreased from the max of 5.5 A in discrete steps until the thruster goes unstable at 1.65 A. From 5.5 A until 2.1 A, the thruster is in local mode and transitions to global mode below 2.1 A. From 2.1 A to 1.75 A the thruster is more oscillatory in global mode, but is stable at the higher mean discharge current value. Below 1.75 A, the discharge current begins to steadily rise and significant fluctuations are seen even on the 1 Hz telemetry without any thruster setting changes as seen for 1.65 A, which is unstable operation.

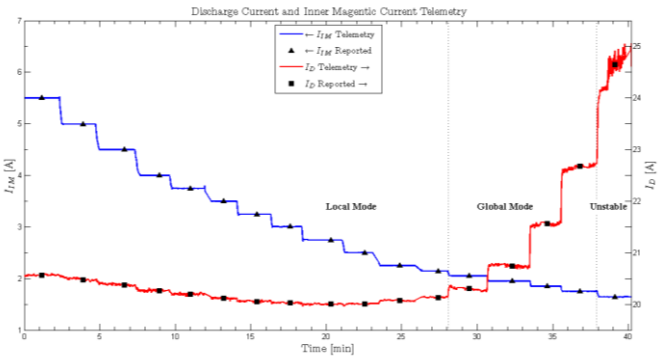

Figure 13 Telemetry for discharge current and inner magnet current for a B-field sweep at 300 V, 19.5 mg/s recorded at 1 Hz. The reported values used in Figure 11(a) and Figure 12(a) are shown as symbols. The B_r/B_r^* regions of local mode, global mode and unstable operation are noted.

B. High-Speed Imaging and Spokes

FastCam videos were acquired of the thruster at all B_r/B_r^* settings during a B-field sweep and were time synchronized with discharge current measurements. All videos were processed as described in Section III A in order to generate a discharge current density surface as shown in Figure 15. Figure 14(a) compares a sample 0.5 ms of a $\hat{I}(t)$ signal, the $\hat{I}(t)$ signal filtered and down-sampled to the camera frame rate of 87.5 kHz with an AC-coupled, normalized m_0 from the FastCam. The original $\hat{I}(t)$ in Figure 14(a) shows higher frequency discharge current oscillations that are not captured with FastCam. The difference between the $\hat{I}(t)$ signal and $\hat{I}(t)$ signal filtered and down-sampled yields the uncertainty $\sigma_{j_{D_b}3}(t)$ in equation (17). The correlation is visually apparent with a linear correlation coefficient of 0.92 between the down-sampled $\hat{I}(t)$ signal and m_0. A linear correlation coefficient of 0.8 or higher is always observed between I_D and m_0, supporting the assumption made in Section III A that the time varying light intensity within the discharge channel is related to the discharge current. The Power Spectral Density (PSD) of the down-sampled $\hat{I}(t)$ and m_0 are nearly identical as shown in Figure 14(b). Therefore, PSDs of the discharge current from the split core hall probes and m_0 spoke order from HIA are excellent proxies for each other and are important comparisons during mode transitions.

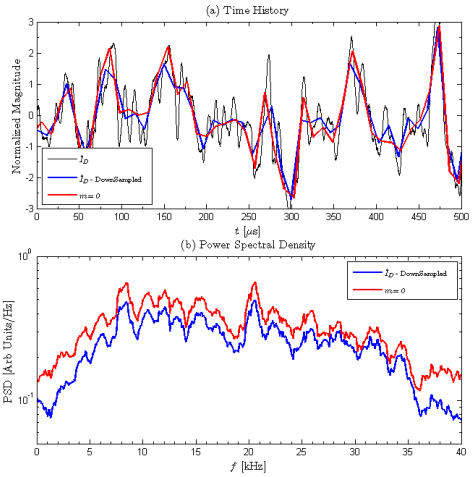

Figure 14 Comparison of normalized, AC-coupled discharge current measurements to m=0 spoke order from FastCam analysis. (a) The time history of the discharge current signal shows higher frequency components than the m=0 signal, but the down-sampled discharge current and the m=0 signal are well correlated, ρ = 0.92. (b) PSD of the down sampled discharge current and m=0 signal also match well. A 1 kHz moving average filter has been applied to smooth both PSDs.

During B-field sweeps HIA analysis of the discharge current density surface shows a distinct change in the discharge channel oscillations as shown in Figure 15 where the transition point is $B_r/B_r^* = 0.60$. While in local mode (higher B_r/B_r^*), the spoke surfaces in the right plots show clear diagonal stripes indicative of strong, coherent spokes or azimuthally propagating perturbations. Figure 15 shows the discharge current mean and RMS values with HIA during the B-field sweep and mode transition for 300V, 19.5 mg/s, where the nominal discharge current is 20 A or 133 mA/cm^2 discharge current density.

Several important features can be distinguished on the discharge current density surface plots, beginning with the low magnetic field setting of $B_r/B_r^* = 0.51$. Vertical stripes of constant current density indicates the entire discharge channel is acting in unison with minimal azimuthal non-uniformities as shown clearly in $B_r/B_r^* = 0.51$. The fluctuations are large with the entire discharge channel at 70 mA/cm^2 (10.6 A) or approximately half of the nominal value at the minimums and then rising to over 300 mA/cm^2 (45 A) during the peak. In 1 ms of the discharge current density surface shown, 8.5 cycles are visible corresponding to a frequency of 8.5 kHz, which is clearly seen as a peak for m = 0 in the above PSD with corresponding harmonics. Other than the m = 1 spoke order (which is just bleed through from m = 0), no spokes are observed to have any significant peaks for $B_r/B_r^* = 0.51$. The PSD peak in m_0 is over 10^7; 2 orders of magnitude higher than the transition point ($B_r/B_r^* = 0.60$) or higher B_r/B_r^* values.

At the transition point, $B_r/B_r^* = 0.60$ in Figure 15, strong vertical stripes are seen between 0.5 and 0.7 ms as well as 0.9 ms, indicating an oscillation in the entire channel. However, diagonal stripes are clearly visible from 0 to 0.5 ms with oscillations between 115 to 150 mA/cm^2, which are nicely symmetric about the mean of 133 mA/cm^2 for the discharge current of 20 A. These diagonal stripes represent azimuthal spokes propagating around the channel counter-clockwise, which is the E×B direction for the H6. The spokes extend for ¼ to ½ of the discharge channel before dissipating and last from 100 to 200 μs in duration. The existence of spokes and global channel oscillations simultaneously indicates the thruster is switching or "bouncing" between the different oscillatory modes. The PSD shows the magnitude of the global mode has decreased by 2 orders of magnitude and is now 11 kHz. Spoke orders 3 through 6 are present, with 4 and 5 the most dominant at 13 and 18 kHz, respectively.

For the nominal magnetic field of $B_r/B_r^* = 1.00$ in Figure 15, very few global oscillations are seen as evidenced by the very flat m_0 in the PSD and only hints of vertical lines in the spoke surface. Spoke orders 3 through 6 are also present with 4 and 5 still the most dominant, but they have shifted down to 10 and 15 kHz, respectively. The spokes are stronger as evidenced by the higher PSD peaks, but also the length of the diagonal lines in the spoke surface. Spokes typically propagate over ½ to sometimes even the entire discharge channel lasting for several 100's μs. The

local oscillations represented by spokes are also from 115 to 150 mA/cm^2 which is about the mean of 133 mA/cm^2 or 20 A.

For the high magnetic field of B_r/B_r^* = 1.57 in Figure 15 the entire discharge channel occasionally "flickers" in or out (i.e. 0.35 ms and 0.65 ms), but is not nearly as periodic as B_r/B_r^* = 0.51. The current density during these peaks can be as high as 180 mA/cm^2. Therefore, the m_0 mode is stronger than B_r/B_r^* = 1.00, but the PSD peak is much broader than B_r/B_r^* = 0.60 or 0.51 since the "flicker" is more sporadic and not at one frequency. The spoke orders 4 through 8 are nearly the same level, with 4 and 5 shifting down again to 9 and 14 kHz, respectively. The spoke peaks are an order of magnitude lower than B_r/B_r^* = 1.00 indicating weaker spokes. As seen qualitatively in the spoke surface, the spokes are "choppy" so there are more spokes present (higher spoke order) but propagate for shorter periods (lower PSD peaks).

In summary, B-fields below the transition thresholds do not support spoke propagation or local oscillations and the entire discharge channel oscillates in unison. At the transitions points, spokes are able to propagate but the channel also occasionally reverts to global oscillation mode so both modes are present. At the nominal B-field strong spokes dominate that are able to propagate over large regions of the discharge channel and global oscillations are minimized. For higher B-field more spokes are present (higher m number in plots) but are less stable (occur for less time before disappearing in spoke surface). As B-field increases, the peak frequency of each mode order also increases, which supports an inverse relation between spoke frequency (i.e. spoke velocity) and B-field.

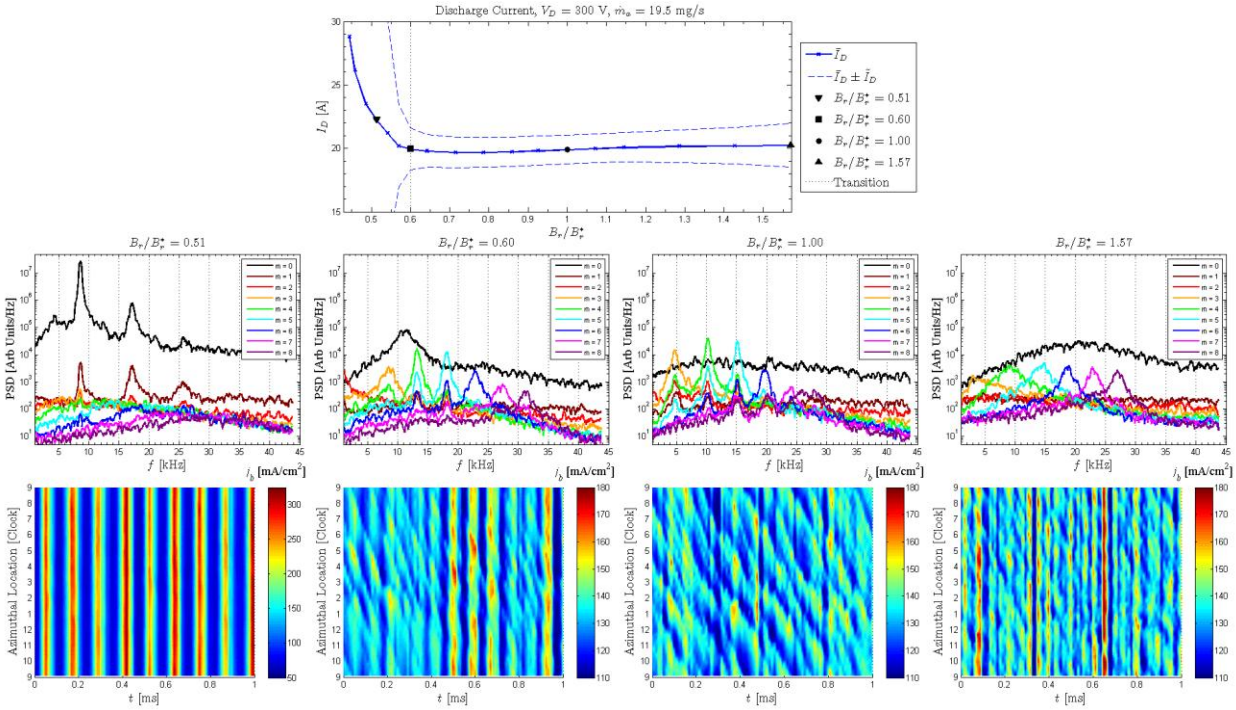

Figure 15 B-field sweep for 300 V, 19.5 mg/s showing transition at B_r/B_r^* = 0.60. The discharge current mean and oscillation amplitude are shown with the transition and for B_r/B_r^* settings selected for further analysis. The middle row plots are FastCam PSDs and the bottom row plots are spoke surfaces. The discharge current density scale range for B_r/B_r^* = 0.51 discharge current density surface is larger due to the magnitude of fluctuations. A 500 Hz moving average filter has been applied to smooth all PSDs.

C. Probe Response

The two HDLP-ISR were positioned in front of the thruster at 6 o'clock for a B-field sweep at 400 V, 19.5 mg/s as shown in Figure 8 with the results shown in Figure 16. The mode transition occurs at B_r/B_r^* = 0.69 where the oscillation amplitude increases greatly below that point. Unlike the 300V case, for high B_r/B_r^* = 1.57 the oscillation amplitude $\tilde{I}_D$ is also quite large at 5 A or 25% of $\bar{I}_D$. The results reported below only use the ion saturation current signals from the ISR probes (I_{ISR}), although high speed data was collected from the HDLP. Simply looking at signal correlation and PSDs, the ISR signals are easier to use with less noise and uncertainty than the high speed electron density, electron temperature or plasma potential results. The same scale fact of 10^5 used in Figure 17 will be applied to the I_{ISR} signal before calculating PSDs in Figure 16 for a direct comparison to discharge current PSDs.

For the global oscillation mode, B_r/B_r^* = 0.60, the discharge current and m = 0 PSDs have a flat peak between 6.6 to 8.5 kHz that is over 1 order of magnitude larger than B_r/B_r^* = 0.69 for m = 0 and almost 2 orders of magnitude larger for the discharge current; both are over two orders of magnitude larger than B_r/B_r^* = 1.00. No spokes are present from HIA or the ISR signals. The discharge current signal peak is larger than the ISR signals indicating the dominance of the global oscillations. At the transition point, B_r/B_r^* = 0.69, spokes are present with m = 4 and 5 dominant at 12 and 17 kHz, respectively, with m = 6 present at 22 kHz and m = 7 present at 27 kHz one order of magnitude lower. The discharge current and m = 0 peaks have shifted to a sharp peak at 9 kHz. The ISR signals show the same peaks as the HIA spokes at 17, 22 and 27 kHz (the 12 kHz peak is weakly present), but the discharge current peak at 9 kHz is entirely absent. This shows local plasma oscillations due to spokes dominate over the global discharge current oscillations. The HIA spoke signals are an order of magnitude lower than the discharge current signal at B_r/B_r^* = 0.69, but the ISR signal is stronger than the discharge current.

At the nominal magnetic field, B_r/B_r^* = 1.00, the discharge current and m = 0 signals have a very broad peak between 15 and 20 kHz. On the HIA PSDs, the dominant spoke orders are m = 3, 4, 5 and 6 at 4, 10, 15 and 19 kHz, respectively, with the m=7 mode 24 and m=8 at 28 kHz also weakly present. The ISR signals have strong peaks at 15, 20 and 24 kHz matching the m=5, 6 and 7 spoke orders well. There is also a broad signal staring at 28 kHz matching m = 8 and extending to 40 kHz which may be caused by the global discharge current. For a higher magnetic field, B_r/B_r^* = 1.29, the discharge current oscillations increase as evidenced by large (same magnitude as transition) and more peaked discharge current and m = 0 order at 20 kHz. On the HIA PSDs, the m=4 spoke order has faded, but m=5, 6, 7 and 8 have peaks at 15, 19, 24 and 28 kHz, respectively. The ISR signals show the same peaks with the strongest peaks at 19 and 24 kHz matching the m = 6 and 7 spoke orders. The peaks have shifted to lower frequencies, but by less than 0.5 kHz and all frequency peaks are rounded to the nearest kHz.

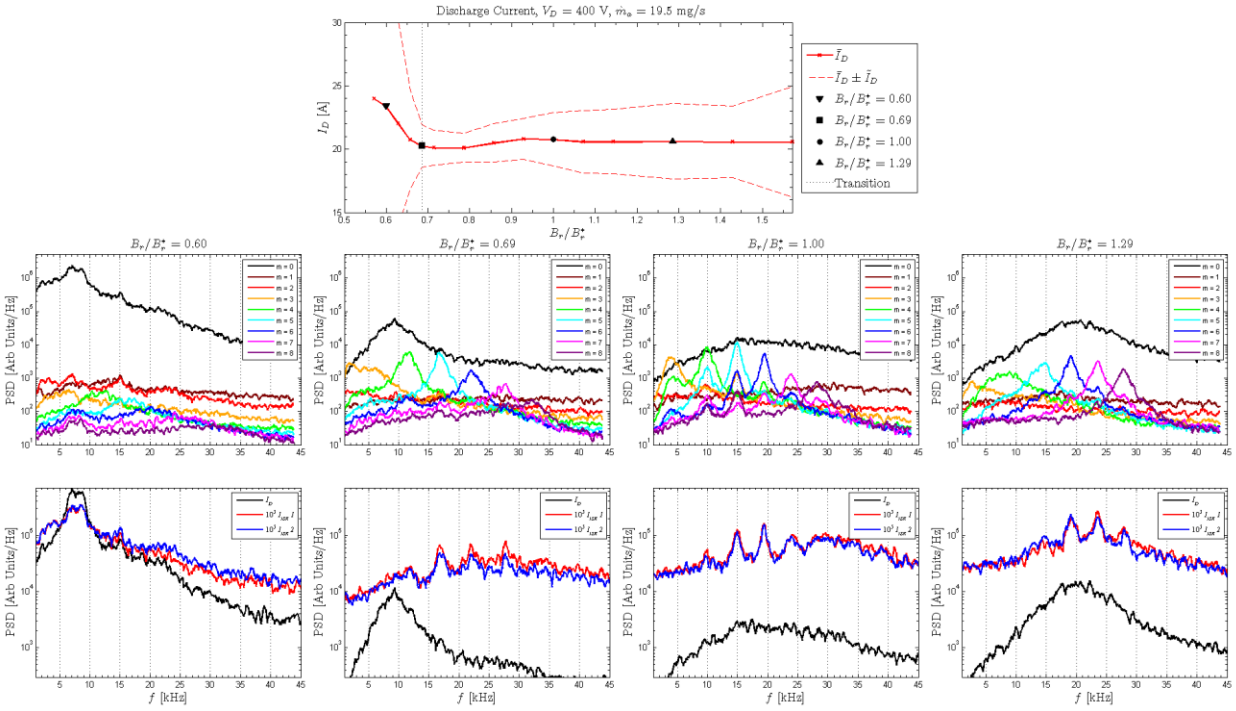

Figure 16 B-field sweep for 400 V, 19.5 mg/s with probes in place showing transition at B_r/B_r^* = 0.69. The discharge current mean and oscillation amplitude are shown with the transition and for B_r/B_r^* settings selected for further analysis. The middle row plots are FastCam PSDs and the bottom row plots are discharge current and ISR signal PSDs. A 500 Hz moving average filter has been applied to smooth all PSDs.

In summary, the PSD for ISR 1 and 2 always match indicating they record the same plasma oscillations. This is important when doing the correlation later as it is shown they do not see the plasma oscillations at the same time. The ISR signals have peaks matching the HIA PSD peaks for spokes with the strongest peaks corresponding to the higher spoke orders. As with the 300 V case, the peak spoke orders m increase with increasing B_r/B_r^* but the frequency of the peaks gradually decreases. No spokes are present in global oscillation mode for ISR signals or HIA PSD. As was hypothesized by Sekerak [27], this indicates that in local oscillation mode, the plasma density

fluctuations are determined by local oscillations within the discharge channel and not a global phenomenon. In global oscillation mode, the entire channel is oscillating in unison.

In order to further investigate the idea of local plasma oscillations versus global oscillations, a time history segment of the discharge current and ISR signals are shown in Figure 17 for local oscillation mode ($B_r/B_r^* = 0.71$) and global oscillation mode ($B_r/B_r^* = 0.60$). The ISR current (I_{ISR}) which is typically of order 100's μA has been scaled by 10^5 and AC-coupled in order to match the AC-coupled discharge current $I_{D_{AC}}$ for $B_r/B_r^* = 0.60$. The difference in the discharge current between the two modes in Figure 17(a) and (b) is also apparent with the local oscillation mode exhibiting lower mean and oscillation amplitude (RMS value) as shown in Table 2. The peak-to-peak value for the time segment shown in Figure 17(a) is less than 6 A for local mode, while the peak-to-peak value for the time segment shown in Figure 17(b) is ~35 A for global mode.

Table 2 Discharge current mean and oscillation amplitude for Figure 17.

	Local Mode	Global Mode
B_r / B_r^*	0.71	0.60
$\bar{I}_D$ [A]	20.1	23.4
$\tilde{I}_D$ [A]	1.4	11.0

For local oscillation mode, Figure 17(a), the linear correlation coefficient ρ between I_{ISR1} and $I_{D\,AC}$ is only 0.23, whereas in global oscillation mode, Figure 17(b) ρ = 0.77. This means I_{ISR1} tracks $I_{D\,AC}$ very well in global oscillation mode, but not in local oscillation mode. In other words, the plasma oscillations in local oscillation mode are independent of the discharge current oscillations, but are not independent in global oscillation mode. The time delay calculated by cross-correlation from I_{ISR1} to I_{ISR2} is 14.7 μs, with an estimated uncertainty of less than 1 μs based on the width of the correlation function. Figure 17(c) shows I_{ISR2} shifted to match I_{ISR1} demonstrating the signals are very well correlated; the correlation coefficient before the time shift was -0.28 and after was 0.52. This means the ISR2 probe sees the same plasma oscillations as ISR1, but delayed by 14.7 μs. The ISR2 probe signal delay is in the spoke propagation direction (E×B direction) from ISR1 leading to the conclusion that the plasma oscillations are caused by the passage of azimuthally propagating spokes as discussed in [27].

For global oscillation mode, Figure 17(b), the time delay calculated by cross-correlation from I_{ISR1} to I_{ISR2} was -1.4 μs, just above the margin of error and the correlation coefficient ρ without time shifting was 0.75 so effectively there was no delay between ISR signals. However, the time delay calculated by cross-correlation from I_{ISR1} to $I_{D\,AC}$ was 9.7 μs, which can be construed as the ion time of flight from the discharge channel to the probes. This means the plasma oscillations occurred uniformly within the discharge channel during surges in discharge current and propagate downstream to be detected by both probes simultaneously.

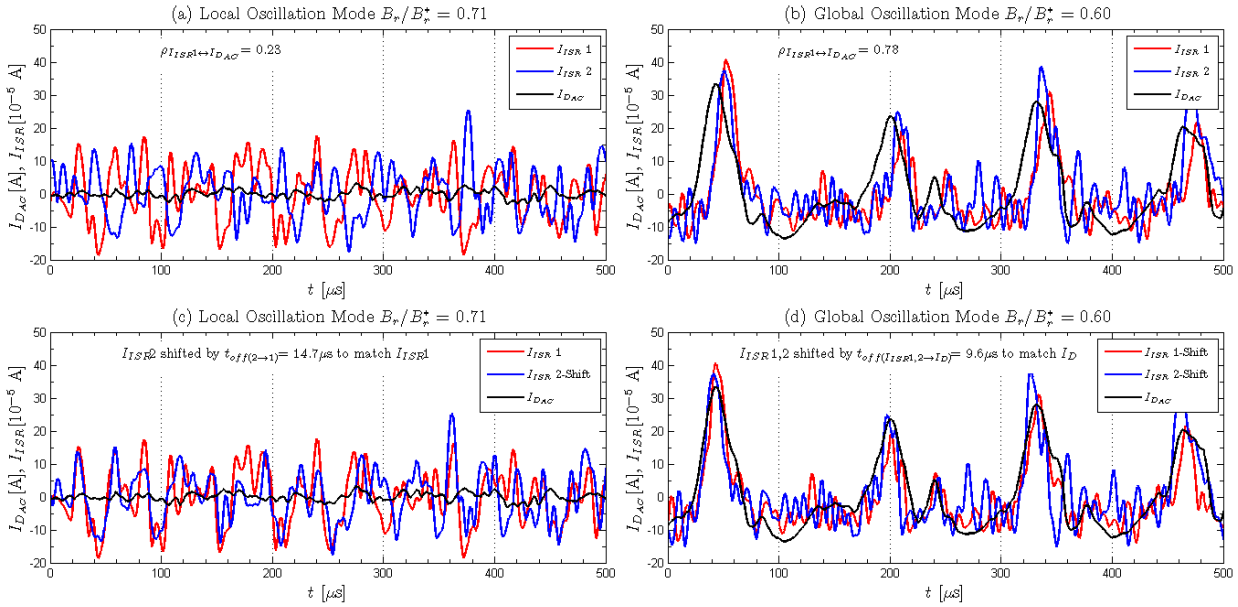

Figure 17 Comparison of AC-coupled discharge current ($I_{D\,AC}$) to AC-coupled ISR current (I_{ISR1} and I_{ISR2}) for 400 V, 19.5 mg/s. Note the I_{ISR} signals have been scaled by 10^5, the I_{DAC} signals are true scale. The ISR signals were low-pass filtered at 150 kHz using a Butterworth 3rd order filter to reduce noise.

The key features identified in Figure 17 of time offsets from discharge current to ISR probes with correlation coefficients and between ISR probes are shown in Figure 18 for 300 V and 400 V, 19.5 mg/s during B-field sweeps. Figure 18(a) shows the discharge current mean and oscillation amplitude with transition points during B-field sweeps, noting that 400 V transitions at a higher B_r/B_r^*. The correlation coefficients ρ in Figure 18(b) are between the AC-coupled I_{ISR1} and $I_{D\,AC}$ after time shifting I_{ISR1} by the offset times shown in Figure 18(d) that are calculated from cross-correlation. Figure 18(b) clearly shows for all B_r/B_r^* values in local oscillation mode, the ISR signal is not well correlated with the discharge current signal as was shown in Figure 17. Below the transition value for B_r/B_r^* the signals become well correlated in global oscillation mode with $\rho > 0.3$. The offset time increases below the transition point for both 300 V and 400 V as shown in Figure 18(d) indicating a longer ion time of flight from the discharge channel to the probes in global mode.

The time offset from ISR1 to ISR2 calculated from cross-correlation is shown in Figure 18(d) where above the transition point the time delay is between 10 and 15 μs. The time delay is generally decreasing with increasing B_r/B_r^* for 400 V, but is relatively constant for 300 V. For both discharge voltages, below the transition point the offset time drops to within ± 3 μs of 0 μs indicating the probes are measuring plasma oscillations nearly simultaneously. Combined with the high correlation coefficient between ISR1 and the discharge current, this indicates the plasma is oscillating in unison within the discharge channel and propagating downstream to be detected by the probes. For 300 V, the offset time does not immediately go near zero indicating some spoke propagation in global oscillation mode during the transition region of $B_r/B_r^* = 0.57$ to 0.60.

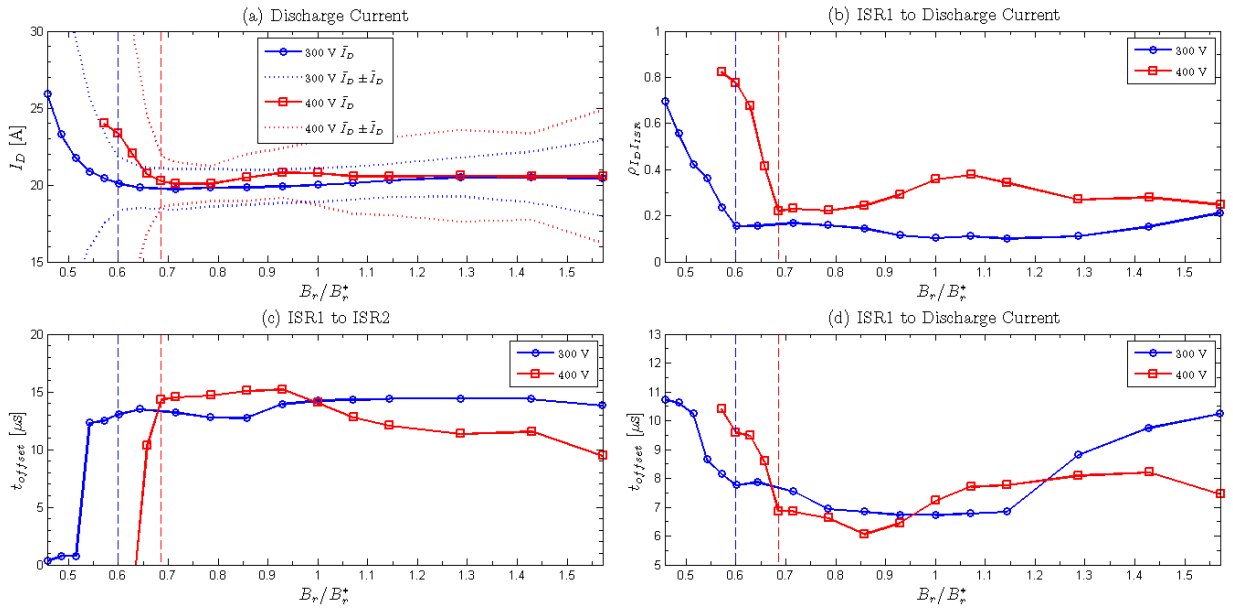

Figure 18 B-field sweeps at 19.5 mg/s for 300V (blue) and 400 V (red) with ISR probes; transition points are shown as vertical dashed lines. (a) Discharge current mean values with oscillation amplitude in dotted lines. (b) Correlation coefficient from ISR1 to discharge current. (c) Time offset from ISR1 to ISR 2 calculated from cross-correlation (d) Time offset from ISR1 to discharge current calculated from cross-correlation.

D. Thrust Measurements

Thrust was measured during B-field sweeps with the results for 300 V, 14.7 mg/s shown in Figure 19. The mean value for the thrust is 281 mN with a standard deviation of 3 mN, which is within the error of 7 mN or 2.5% of the mean value. Therefore, the thrust was constant within experimental error during the B-field sweep. The discharge current, however, increased below the transition point at B_r/B_r^*= 0.53 from 14 A to 19 A at B_r/B_r^*= 0.39. With a constant discharge voltage of 300 V, the increase in discharge current indicates an increase in power to the thruster so the thrust to power (*T/P*) decreases significantly in global oscillation mode. The peak T/P of 67 mN/kW occurs between B_r/B_r^* = 0.64 and 0.79 and decreases to 50 mN/kW at the minimum magnetic field representing a 25% decrease in T/P.

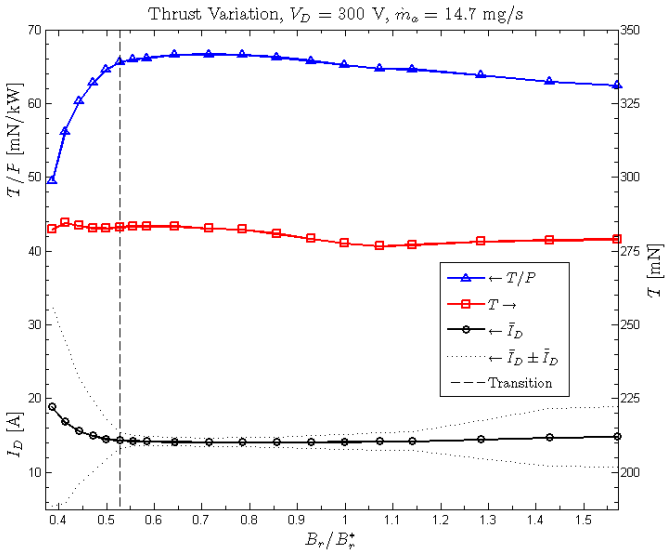

Figure 19 Thrust and T/P for 300 V, 14.7 mg/s during B-field sweep. The thrust is constant at 281 mN within experimental error, but the T/P decreases below the transition point as the discharge current increases.

E. Plume Photos

Nearly profile digital photographs were taken of the thruster at each B_r/B_r^* setting in order to qualitatively show the plasma plume evolution during mode transitions as shown in Figure 20. The viewing angle was angled slightly upstream so the discharge channel was visible very obliquely. The photos with accompanying contours were modeled after Figure 1 of Brown [12] which also qualitatively showed plume shape changes between modes. The contours show relative light intensity calculated from a grayscale version of the image where 1 is the brightest and 0 is dark. Note the probes can be seen as vertical lines of intensity ~0.2 in the plume at 1.5 channel radii downstream near the bottom of the picture and should be disregarded. Visible brightness is important because it indicates excited energy states caused by collisions. The brighter a region, the more collisions are occurring causing excited electron states which then decay emitting light. So although qualitative, the brightness of the plume is representative of the plasma physics occurring in the near-field region. Here we define the near-field

plume region as the plasma directly downstream from the discharge channel a few channel widths. The far-field plasma is the plasma outside of the near-field region.

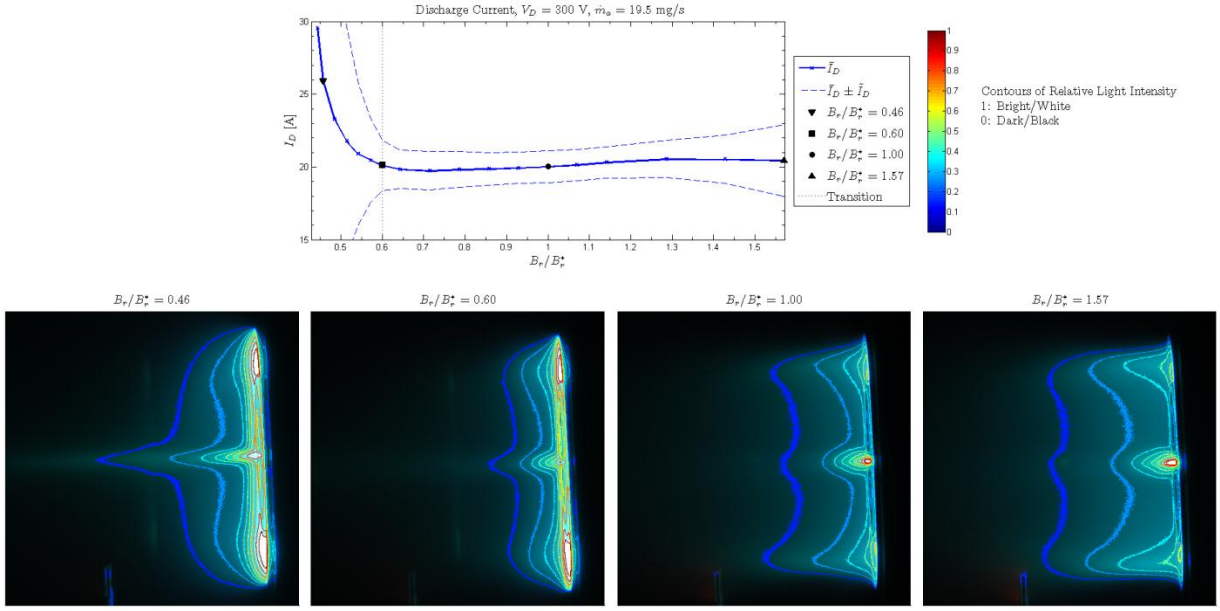

Figure 20 Plume photos showing light intensity during B-field sweep with the internal cathode at 300 V, 19.5 mg/s. Contours of relative intensity are shown to qualitatively illustrate the change in plume shape. Note the probes are present 1.5 channel radii downstream at the bottom and should be disregarded.

In global oscillation mode where B_r/B_r^* = 0.46, the discharge channel is very bright with relative intensity 1 and the center spike of plasma extending along thruster centerline. The spike extends downstream over 1 channel diameter and dominates the plume. As B_r/B_r^* is increased to 0.60 at the transition point, the center spike recedes but the discharge channel is still very bright at 1. At the nominal magnetic field setting, B_r/B_r^* = 1, where the thruster is in localized oscillation mode, the center spike is not present although the plasma from the cathode is still visible on centerline. The relative light intensity visible in the channel is only 0.6 to 0.7 which means the near-field plasma is less collisional and the collisions are likely occurring deeper within the channel where they are not visible to the camera. At B_r/B_r^* = 1.57, the discharge current oscillation amplitude is greater and the plume is again brighter downstream, but the channel relative brightness is still only 0.6 to 0.7. In general, the plume receding as B_r/B_r^* is increased from global oscillation mode to local oscillation mode indicating less collisions and other processes are occurring within the near-field plume and are more confined to within the discharge channel.

The same B-field sweep was conducted with the cathode mounted externally as shown in Figure 21. For the low magnetic field setting, B_r/B_r^* = 0.47, the plume brightness extends downstream with the central spike dominating the plume structure. As B_r/B_r^* is increased to 0.56, the plume recedes towards the channel with some vestige of the center spike remaining. Both settings are in the global oscillation mode and the discharge channel relative brightness is 1. Increasing B_r/B_r^* above the transition point into local oscillation mode the center spike disappears and the discharge channel relative brightness is only 0.6 to 0.7. The transition point for the external cathode case is at a higher B_r/B_r^* = 0.65 setting than the internal case B_r/B_r^* = 0.60. The plume now extends out primarily along the channel indicating the plasma is well focused from the discharge channel downstream. Note the probes are present at the bottom and a reflection from the LVTF viewport sacrificial glass is visible as a vertical perturbation 1 channel radii downstream, both should be disregarded. For the external cathode case at 300 V, 19.5 mg/s, B_r/B_r^* was first swept from 1.57 to minimum and then increased again showing repeatability; the photos shown in Figure 21 are during the initial down sweep.

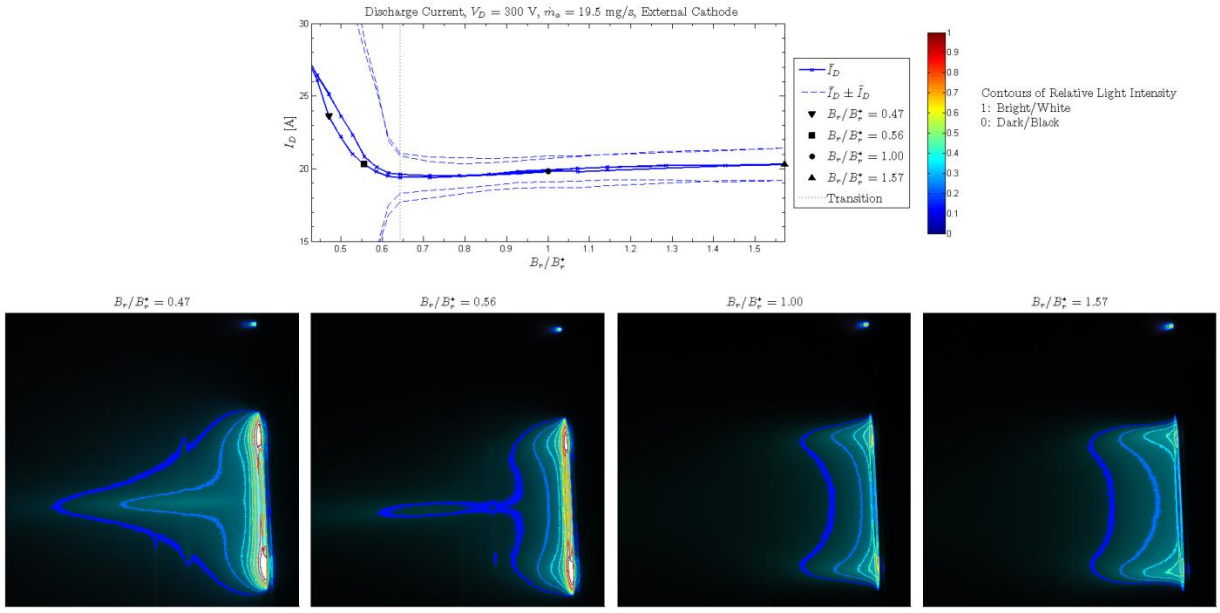

Figure 21 Plume photos showing light intensity during B-field sweep with the external cathode at 300 V, 19.5 mg/s. Contours of relative intensity are shown to qualitatively illustrate the change in plume shape. The probes are present at the bottom and a reflection from the LVTF viewport sacrificial glass is visible as a vertical perturbation 1 channel radii downstream, both should be disregarded. Br/Br* was first swept from 1.57 to minimum and then increased again. The cathode is visible above the thruster at the 12 o'clock position.

VI. Discussion

The results shown above are significant in the description and definition of the commonly observed mode transitions. While the results do not answer the question of whether the mode transitions are wall-effect phenomena as stated by Gascon and Barral or a near-field plume effect as suggested by the work of Brown, they do provide valuable insight into HET operation.

A. Definitions of Modes

Here we define the modes by their plasma oscillation characteristics where most conditions should be satisfied to represent either mode. An attempt is made to quantify the mode metrics, but the criteria values are meant only as a guide and not rigid discriminators. These criteria are based on the above observations of the H6 and are likely different for other HETs, but since mode transitions have been observed in other thrusters a subset of the criteria below should apply.

Global Oscillation Mode The discharge current density in the entire channel is oscillating in unison with peak values of order 100% of the mean value and azimuthally propagating perturbations are either entirely absent or of negligible magnitude with respect to the discharge current density peaks. The m_0 mode of the HIA PSD has a clearly defined peak value and spoke orders m > 1 do not have peaks more than an order of magnitude above the general noise floor. Azimuthally spaced probes do not observe delays in plasma property oscillations indicative of the entire channel oscillating in unison, and are well correlated to the discharge current with $\rho > 0.3$. The discharge current oscillation amplitudes (RMS) are well above 10% of the mean discharge current value and the mean discharge current is over 15% higher than the minimum discharge current value obtained in a sweep. The discharge channel and near-field plume regions are observed to be brighter indicative of increased collisions in the plume; a spike of bright plasma is visible on thruster centerline.

Local Oscillation Mode The discharge current density oscillations are dominated by localized perturbations that are less than 25% of the mean value and propagate in the E×B direction. Oscillations may be present where the entire channel increases or decreases in unison, but they are sporadic and do not dominate the azimuthal propagations. The m_0 mode of the HIA PSD has a very broad peak value and spoke orders m > 1 have peaks more than an order of magnitude above the general noise floor. Azimuthally spaced probes observe clear delays in plasma property oscillations indicative localized regions of increased ionization within the discharge channel propagating downstream. The probe signals are not well correlated to the discharge current with $\rho < 0.3$. The discharge current oscillation amplitudes (RMS) are less than approximately 10% of the mean discharge current value and the mean

discharge current is within 15% of the minimum discharge current value obtained in a sweep. The discharge channel and near-field plume regions are observed to be dimmer indicative of decreased collisions in the plume and collisional processes more confined to within the discharge channel. The plasma is well focused on discharge channel centerline and the center spike of plasma is absent for an external cathode or greatly diminished for an internal cathode; an internal cathode will always produce a spike on thruster centerline because it is a plasma source.

The above definitions clearly delineate the thruster behavior when in either mode, but a transition region exists between modes which is less defined. In this transition region, the thruster does not meet all of the criteria for either mode and the HIA clearly shows the thruster jumping between modes as evidenced from $B_r/B_r^* = 0.60$ in Figure 15.

B. Role of Spokes in Anomalous Electron Transport and Mode Transitions

The results from azimuthally spaced probes supports the ideas presented in [27] where rotating azimuthal non-uniformities (spokes) are azimuthally propagating regions of increased ionization producing a helical structure within the plasma. The regions of increased ionization propagating in the E×B direction would cause a delay between probe signals as illustrated in Figure 22. Spokes are dominant in local oscillation mode but absent in global oscillation mode where the probe signals show negligible time delay and are very well correlated to the discharge current. HIA also supports local versus global oscillations within the discharge channel. Extrapolating these results from the H6 to all annular HETs with similar magnetic field topologies such as the SPT-100, they should be operated in a mode where spokes are present because it increases thruster performance be decreasing discharge current.

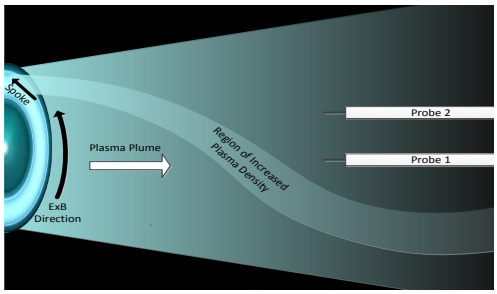

Figure 22 Illustration of spokes as regions of increased ion density producing helical structures of increased plasma density within the plume and how that would be measured by azimuthally spaced probes. Reproduced from Figure 12 of [27].

As shown in Figure 19 thrust is constant, but $\bar{I}_D$ increases so extrapolating from Brown's work [12] the electron transport increases during transitions from local mode to global mode. The implication is that the presence of spokes indicates *decreased* electron transport to the anode. This raises an interesting causality question of whether the presence and mechanics of propagating spokes reduces electron transport to the anode or the plasma conditions that decrease electron transport also allow spokes to propagate. Regardless, the presence or disappearance of spokes is related to electron transport and strong spoke behavior is a symptom of higher efficiency operation and should be sought after.

Spokes have been thought of as possible current carrying mechanisms to explain anomalous electron transport. Janes and Lowder [36] suggested that azimuthal electric fields from spokes could produce E×B drift in axial direction and could account for anomalous electron transport. Recent work on a Cylindrical Hall Thruster (CHT) [37, 38] has demonstrated that 50% of the discharge current is carried through a spoke (only one spoke is observed in the CHT). While CHT results have questionable relevance due to the significant difference in geometry (no inner channel wall) and magnetic field topology versus the H6, SPT-100 or any traditional annular discharge channel, they do reinforce to the idea that significant current can pass through a spoke. Unfortunately, it was also reported that the CHT performance (measured by discharge current) increased when the spoke was *not* present [39], which is opposite of what has been clearly shown in this work. Here electron transport decreases when spokes are present and based on these results thrusters should be operated in local oscillation mode. Spokes cannot be the sole cause for anomalous electron transport because they are not present in global mode where electron transport is higher. Spokes are localized oscillations that are typically 10-20% of the mean discharge current density value while the global oscillation mode can be 100% of the mean value as shown in Figure 15. It is difficult to explain how a 10-20% oscillation can cause the order of magnitude higher electron transport than predicted by classical theory or Bohm diffusion [40]. A one-size fits all description for causes of anomalous electron transport is improbable and likely several different mechanisms are at work.

The question raised in Section II is whether wall effects or near-field plume properties were a cause for mode transitions and the presence or disappearance of spokes between modes may be an important clue. The photographs of Figure 20 and Figure 21 clearly show a change in light intensity in the near-field plume region after mode transition; however this does not prove causality. A possible explanation can be made from the wall-effect theory of Gascon and Barral [7, 8] where the transition occurs when the discharge channel wall enters space charge saturation. As was discussed by King [41] based on single particle motion, the electrons cannot move around the thruster in a

perfectly circular path due to the cylindrical geometry, but must reflect off the walls to stay in the azimuthal hall current If the wall is in space charge saturation, then it may not be able to reflect the electrons back into the hall current before they escape to the anode. This implies that the rotating spoke is caused by azimuthal motion of electrons in the hall current and will be the subject of a future publication.

C. Thruster Performance

The minimum mean discharge current typically occurred in local mode right before the transition region as shown in Figure 11 and Figure 12. Similarly, the peak *T/P* occurs near the transition point in Figure 19 where the thruster is on the verge of entering global oscillation mode. If one were to choose magnetic field settings for flight operation based on maximizing *T/P* or minimizing $\bar{I}_D$, then the thruster would be operating near the transition point where any perturbation in magnetic field (due to pole piece B-H properties changing over time, magnetic coils degrading, etc) or changes in wall geometry and properties (due to erosion, coating from sputtered material, etc) during the mission could cause the thruster to be more sensitive to transitioning from localized oscillation mode to global oscillation mode. The B-field sweeps shown in Figure 11 and Figure 12 were constant and repeatable across several pump downs, but will likely change during the life of the thruster. This is more likely to be true if the transitions are related to wall effects where the plasma properties near the wall (i.e. susceptibility to space charge saturation) may change as the wall erodes. Therefore, these $\bar{I}_D$ I_D vs B_r/B_r^* curves, while very repeatable during this test campaign, are likely only snapshots and may change after 1000's of hours of operation.

VII. Conclusion

Previous researchers have identified mode transitions in HETs where a small change in a thruster operating parameter such as discharge voltage, magnetic field or mass flow rates cause the thruster discharge current mean and oscillation amplitude to increase significantly. Mode transitions in the H6 were induced by varying the magnetic field intensity while holding all other operating parameters constant and measurements were acquired with ion saturation probes and ultra-fast imaging. A technique was developed that calculated discharge current density oscillations from FastCam images of the discharge channel in order to quantify the fluctuations. Spokes are localized oscillations that are typically 10-20% of the mean discharge current density value while the global oscillation mode can be 100% of the mean value.

The modes are described here as global oscillation mode and local oscillation mode. In global mode the entire discharge channel is oscillating in unison and spokes are either absent or negligible with discharge current oscillation amplitude (RMS) greater than 10% of the mean value. Downstream azimuthally spaced probes show no signal delay between each other and are very well correlated to the discharge current signal. In local oscillation mode perturbations in the discharge current density are seen to propagate in the E×B direction with clear spokes shown in a HIA PSD. The discharge current oscillation amplitude and mean values are significantly lower than global mode. Downstream azimuthally spaced probes show a clear signal delay between each other indicating the passage of spokes but are not well correlated to the discharge current indicating localized plasma oscillations within the discharge channel. The mode transitions were consistent across different tests and showed no hysteresis, but did change at different operating conditions. The transition between global mode and local mode occurred at higher relative B-field strengths for higher mass flow rate or higher discharge voltage.

The thrust was constant within experimental error through the mode transition but the thrust to power decreased by 25% for the 14.7 mg/s flow rate; the peak in thrust to power occurs near the transition point. The plume showed significant differences between modes with the global mode significantly brighter in the channel and the near-field plasma as well as exhibiting a plasma spike on thruster centerline. For the external cathode case the plasma spike disappeared in local oscillation mode. Based on the research presented here the H6 should be operated in local oscillation mode to minimize discharge current and maximize performance.

Acknowledgments

The primary author acknowledges this work was supported by a NASA Office of the Chief Technologist's Space Technology Research Fellowship (NSTRF). The authors would like to thank two former PEPL students: Dr. Robert Lobbia for development of the HDLP; and Dr. Michael McDonald for development of the FastCam Analysis.

References

[1] A. I. Morozov, "The conceptual development of stationary plasma thrusters," *Plasma Physics Reports*, vol. 29, no. 3, pp. 235–250, Mar. 2003.

[2] A. I. Morozov, Y. Esipchuk, G. N. Tilinin, A. V. Trofimov, Y. A. Sharov, and G. Y. Shchepkin, "Plasma accelerator with closed electron drift and extended acceleration zone," *Soviet Physics-Technical Physics*, vol. 17, no. 1, pp. 38–44, Jul. 1972.

[3] R. Hofer et al., "Efficacy of Electron Mobility Models in Hybrid-PIC Hall Thruster Simulations," paper no. AIAA 2008-4924, presented at the 44th AIAA/ASME/SAE/ASEE Joint Propulsion Conference & Exhibit, Hartford, CT, 2008.

[4] I. G. Mikellides, I. Katz, R. R. Hofer, and D. M. Goebel, "Magnetic shielding of walls from the unmagnetized ion beam in a Hall thruster," *Applied Physics Letters*, vol. 102, no. 2, p. 023509, 2013.

[5] G. N. Tilinin, "High-frequency plasma waves in a Hall accelerator with an extended acceleration zone," *Soviet Physics-Technical Physics*, Aug. 1977.

[6] N. Yamamoto, T. Nakagawa, K. Komurasaki, and Y. Arakawa, "Influence of Discharge Oscillation on Hall Thruster Performance," paper no. IEPC-01-055, presented at the 27th International Electric Propulsion Conference, Pasadena, CA, 2001.

[7] N. Gascon, M. Dudeck, and S. Barral, "Wall material effects in stationary plasma thrusters. I. Parametric studies of an SPT-100," *Physics of Plasmas*, vol. 10, no. 10, p. 4123, 2003.

[8] S. Barral, K. Makowski, Z. Peradzyński, N. Gascon, and M. Dudeck, "Wall material effects in stationary plasma thrusters. II. Near-wall and in-wall conductivity," *Physics of Plasmas*, vol. 10, no. 10, p. 4137, 2003.

[9] A. V. Baitin, L. I. Elizarov, A. A. Ivanov, and M. Bacal, "Maximum value and stability of near-wall current," presented at the 24th International Electric Propulsion Conference, Moscow, Russia, 1995.

[10] L. Jolivet and J.-F. Roussel, "Effects of the secondary electron emission on the sheath phenomenon in a Hall thruster," presented at the Third International Conference on Spacecraft Propulsion, Cannes, France, 2000.

[11] O. A. Mitrofanova, R. Y. Gnizdor, V. M. Murashko, A. I. Koryakin, and A. N. Nesterenko, "New Generation of SPT-100," paper no. IEPC-2011-041, presented at the 32nd International Electric Propulsion Conference, Wiesbaden, Germany, 2011.

[12] D. Brown and A. Gallimore, "Investigation of Low Discharge Current Voltage Hall Thruster Operating Modes and Ionization Processes," paper no. IEPC-2009-074, presented at the 31st International Electric Propulsion Conference, Ann Arbor, MI, 2009.

[13] M. McDonald and A. Gallimore, "Parametric Investigation of the Rotating Spoke Instability in Hall Thrusters," paper no. IEPC-2011-242, presented at the 32nd International Electric Propulsion Conference, Wiesbaden, Germany, 2011.

[14] R. Hofer, D. Goebel, I. Mikellides, and I. Katz, "Design of a Laboratory Hall Thruster with Magnetically Shielded Channel Walls, Phase II: Experiments," paper no. AIAA 2012-3789, presented at the 48th AIAA/ASME/SAE/ASEE Joint Propulsion Conference & Exhibit, Atlanta, GA, 2012.

[15] B. M. Reid, "The Influence of Neutral Flow Rate in the Operation of Hall Thrusters," Ph.D. Dissertation, Dept. of Aerospace Eng., University of Michigan, Ann Arbor, MI, 2009.

[16] D. L. Brown, "Investigation of Low Discharge Voltage Hall Thruster Characteristics and Evaluation of Loss Mechanisms," Ph.D. Dissertation, Dept. of Aerospace Eng., University of Michigan, Ann Arbor, MI, 2009.

[17] K. K. Jameson, "Investigation of hollow cathode effects on total thruster efficiency in a 6 kW Hall thruster," Ph.D. Dissertation, Dept. of Aerospace Eng., University of California, Los Angeles, Los Angeles, CA, 2008.

[18] R. Shastry, "Experimental Characterization of the Near-Wall Region in Hall Thrusters and its Implications on Performance and Lifetime," Ph.D. Dissertation, Dept. of Aerospace Eng., University of Michigan, Ann Arbor, MI, 2011.

[19] M. McDonald, "Electron Transport in Hall Thrusters," Ph.D. Dissertation, Applied Physics, University of Michigan, Ann Arbor, MI, 2012.

[20] W. Huang, "Study of Hall Thruster Discharge Channel Wall Erosion via Optical Diagnostics," Ph.D. Dissertation, Dept. of Aerospace Eng., University of Michigan, Ann Arbor, MI, 2011.

[21] R. Hofer, I. Mikellides, I. Katz, and D. Goebel, "Wall Sheath and Electron Mobility Modeling in Hybrid-PIC Hall Thruster Simulations," paper no. AIAA 2007-5267, presented at the 43rd AIAA/ASME/SAE/ASEE Joint Propulsion Conference & Exhibit, Cincinnati, OH, 2007.

[22] I. Mikellides, I. Katz, R. Hofer, and D. Goebel, "Hall-Effect Thruster Simulations with 2-D Electron Transport and Hydrodynamics Ions," paper no. IEPC-2009-114, presented at the 31st International Electric Propulsion Conference, Ann Arbor, MI, 2009.
[23] T. W. Haag, "Thrust stand for high-power electric propulsion devices," *Review of Scientific Instruments*, vol. 62, no. 5, p. 1186, 1991.
[24] K. G. Xu and M. L. R. Walker, "High-power, null-type, inverted pendulum thrust stand," *Review of Scientific Instruments*, vol. 80, no. 5, p. 055103, 2009.
[25] R. B. Lobbia and A. D. Gallimore, "High-speed dual Langmuir probe," *Review of Scientific Instruments*, vol. 81, no. 7, p. 073503, 2010.
[26] R. Lobbia, M. Sekerak, R. Liang, and A. Gallimore, "High-speed Dual Langmuir Probe Measurements of the Plasma Properties and EEDFs in a HET Plume," paper no. IEPC-2011-168, presented at the 32nd International Electric Propulsion Conference, Wiesbaden, Germany, 2011.
[27] M. Sekerak, M. McDonald, R. Hofer, and A. Gallimore, "Hall Thruster Plume Measurements from High-Speed Dual Langmuir Probes with Ion Saturation Reference," paper no. IEEE-2013-2129, presented at the 34th IEEE Aerospace Conference, Big Sky, MT, 2013.
[28] B. E. Cherrington, "The use of electrostatic probes for plasma diagnostics - A review," *Plasma Chemistry and Plasma Processing*, vol. 2, no. 2, pp. 113–140, Jun. 1982.
[29] J. D. Swift and M. J. R. Schwar, *Electrical probes for plasma diagnostics*. London; New York: Iliffe Books; American Elsevier, 1969.
[30] J. S. Bendat and A. G. Piersol, *Engineering applications of correlation and spectral analysis*. New York: Wiley, 1980.
[31] M. McDonald, C. Bellant, B. St Pierre, and A. Gallimore, "Measurement of Cross-Field Electron Current in a Hall Thruster Due to Rotating Spoke Instabilities," paper no. AIAA 2011-5810, presented at the 47th AIAA/ASME/SAE/ASEE Joint Propulsion Conference & Exhibit, San Diego, CA, 2011.
[32] M. S. McDonald and A. D. Gallimore, "Rotating Spoke Instabilities in Hall Thrusters," *IEEE Transactions on Plasma Science*, vol. 39, no. 11, pp. 2952–2953, Nov. 2011.
[33] P. R. Bevington and D. K. Robinson, *Data reduction and error analysis for the physical sciences*. New York: McGraw-Hill, 1992.
[34] R. D. Strum, *First principles of discrete systems and digital signal processing*. Reading, Mass: Addison-Wesley, 1988.
[35] A. V. Oppenheim, *Discrete-time signal processing*. Englewood Cliffs, N.J: Prentice Hall, 1989.
[36] G. S. Janes and R. S. Lowder, "Anomalous Electron Diffusion and Ion Acceleration in a Low-Density Plasma," *Physics of Fluids*, vol. 9, no. 6, p. 1115, 1966.
[37] Y. Raitses, M. Griswold, L. Ellison, J. Parker, and N. Fisch, "Studies of Rotating Spoke Oscillations in Cylindrical Hall Thrusters," paper no. AIAA 2012-4179, presented at the 48th AIAA/ASME/SAE/ASEE Joint Propulsion Conference, Atlanta, GA, 2012.
[38] C. L. Ellison, Y. Raitses, and N. J. Fisch, "Cross-field electron transport induced by a rotating spoke in a cylindrical Hall thruster," *Physics of Plasmas*, vol. 19, no. 1, 2012.
[39] J. B. Parker, Y. Raitses, and N. J. Fisch, "Transition in electron transport in a cylindrical Hall thruster," *Applied Physics Letters*, vol. 97, no. 9, p. 091501, 2010.
[40] L. Garrigues, J. Pérez-Luna, J. Lo, G. J. M. Hagelaar, J. P. Boeuf, and S. Mazouffre, "Empirical electron cross-field mobility in a Hall effect thruster," *Applied Physics Letters*, vol. 95, no. 14, p. 141501, 2009.
[41] L. King, "A (Re-)examination of Electron Motion in Hall Thruster Fields," paper no. IEPC-2005-258, presented at the 29th International Electric Propulsion Conference (IEPC), Princeton University, 2005.

Mode Transitions in Hall Effect Thrusters

Michael Sekerak, Benjamin Longmier,
Alec Gallimore, Daniel Brown,
Richard Hofer, James Polk

AIAA Joint Propulsion Conference

San Jose, CA

15-17 July, 2013

HET Oscillations

- Hall Effect Thrusters (HETs)
  - Under development since 1960's; first flew in early 1970's.
  - Physics not fully understood; anomalous electron transport unresolved (many more electrons cross magnetic field lines than expected by classical theory).
  - Cannot develop first principles, predictive models of thruster operation.
- Oscillations
  - Oscillations and modes have been discussed from many early Russian researchers (Morozov, Esipchuk, Tilinin) through reviews (Choueiri) and recent investigations (Raitses, Barral, McDonald).
  - Terms stable and unstable to describe the thruster operation are misleading; HETs can be quite stable (although undesirable) in a highly oscillatory mode.
  - Breathing mode: global depletion and replenishment of neutrals in discharge channel creating axial oscillations.
  - Spoke mode: azimuthally propagating waves in E × B direction.
  - Both are believed to be ionization processes and effect anomalous electron transport as well as performance.

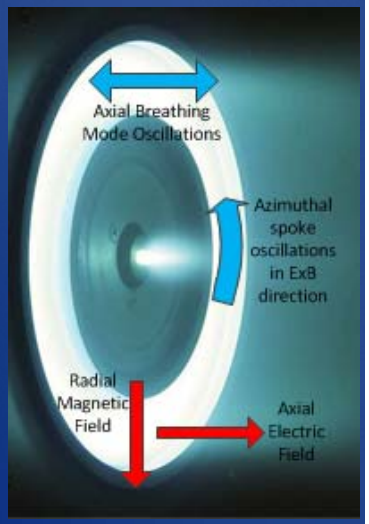

HET showing radial magnetic field, axial electric field and oscillation directions.

Need for Fundamental Understanding of HETs

- Bottom Line: We don't know exactly how HETs work, but we know how to make them work.
- Reasons to determine fundamentals of HET operation:
  - First principles predictive models would enable design of higher performing HETs.
  - Reduce experimental iterations during design phase to save time and cost.
  - Augment and/or reduce life testing so the timeline and associated costs to flight qualify a thruster can be reduced.
  - Ensure that ground testing adequately prepares or predicts thruster operation on orbit (ambient pressures on orbit are orders of magnitude lower).
  - Facilitate scaling of HETs to very high power and or multi-channel Nested Hall Thrusters.
  - Ensure that magnetic shielding and low/zero-erosion concepts are stable.

Mode Transitions

- Brown investigations on H6 for low-voltage operation[1]
  - Transition from high current to low current mode decreased mean and RMS of discharge current; increased efficiency and beam utilization.
  - Increased discharge current caused by increased electron current to anode in high current mode.
  - Ambient neutral density effected transition; lower pressure could induce high current mode.
- Gascon et al investigations of wall material effects in SPT-100[2]
  - Noted transition in modes with varying magnetic field strength (higher discharge current mean value and oscillation amplitude).
  - Discharge oscillations significantly affected by nature of walls.

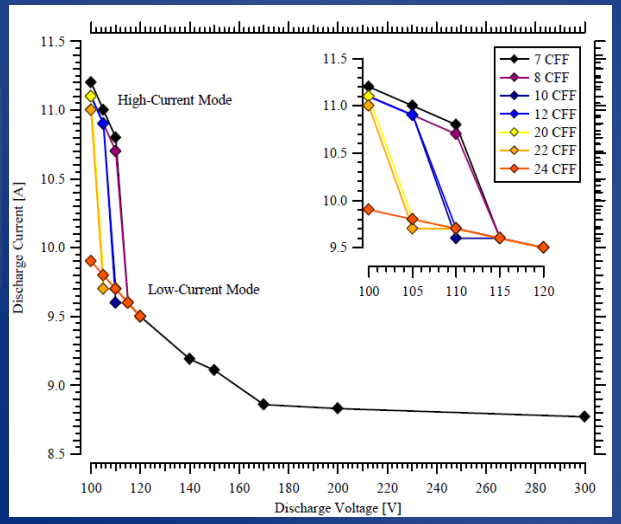

Plume photos from Figure 1 of Brown[1] showing discharge current change between modes.

Thruster efficiency and stability linked to oscillations and modes.

[1] D. Brown and A. Gallimore, "Investigation of Low Discharge Current Voltage Hall Thruster Operating Modes and Ionization Processes," 31st International Electric Propulsion Conference, Ann Arbor, MI, 2009.

[2] N. Gascon, M. Dudeck, and S. Barral, "Wall material effects in stationary plasma thrusters. I. Parametric studies of an SPT-100," *Physics of Plasmas*, 2003.

Transitions due to Near Wall Conductivity

- Transitions noted from wall effect studies.[1,2]
- Theory proposed by Barral using 1-D fluid simulation with analytical solution of presheaths, electron temperature anisotropy, and no experimental transfer mobility coefficients.
- Sheath potential for an insulating wall ($\Delta\Phi_S$) has singularity when secondary electron emission (σ) coefficient goes to 1:

$$\Delta\Phi_S = \frac{kT_e}{e}\ln\left[(1-\sigma)\sqrt{\frac{m_i}{2\pi m_e}}\right]$$

- Called the Space Charge Saturation (SCS) transition where a potential well forms close to wall trapping secondary electrons.
- Increases near wall conductivity to which Barral attributes the increased discharge current.

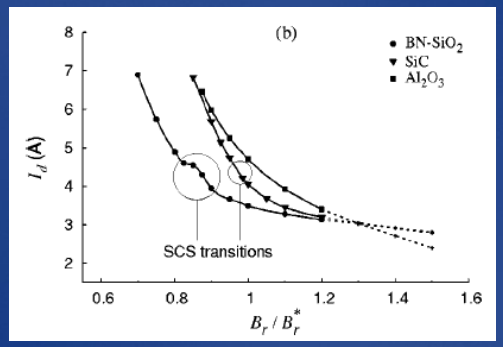

Simulated discharge current from 1-D fluid model with magnetic field variations for different wall materials, Figure 10 from Barral[2]. The steep rise in discharge current is attributed to the space charge saturation transition.

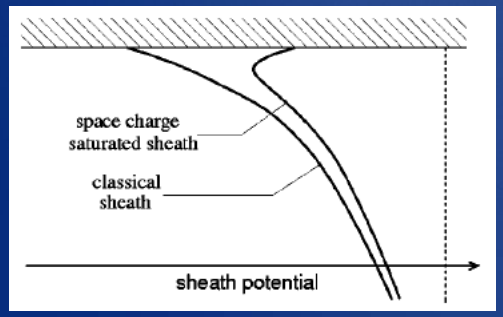

Sheath potential profiles at the wall with and without SCS, Figure 3 of Barral[2].

[1] N. Gascon, M. Dudeck, and S. Barral, "Wall material effects in stationary plasma thrusters. I. Parametric studies of an SPT-100," Physics of Plasmas, vol. 10, no. 10, p. 4123, 2003.
[2] S. Barral, K. Makowski, Z. Peradzyński, N. Gascon, and M. Dudeck, "Wall material effects in stationary plasma thrusters. II. Near-wall and in-wall conductivity," Physics of Plasmas, vol. 10, no. 10, p. 4137, 2003.

HET and Facility

- H6: 6 kW HET
  - Joint development effort by University of Michigan, NASA JPL and AFRL.
  - Very well characterized; 6 experimental dissertations and many papers.
  - Nominal operating condition: 300 V, 20 A (~20 mg/s) with xenon, IM/OM: 3.50/3.13 A.
  - Internal LaB_6 cathode, 7% flow fraction.
  - Well worn rings and slight oxidation present on anode.
- Plasmadynamics and Electric Propulsion Lab (U of M)
  - Large Vacuum Test Facility (LVTF).
  - 9 m long, 6 m diameter chamber.
  - Pumping speed 240,000 L/s on Xe maintaining ~1×10^{-5} Torr during thruster operation.

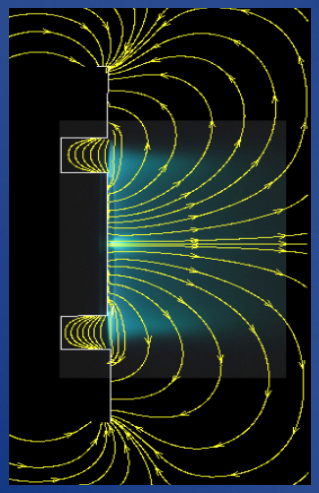

Profile picture of the H6 operating at nominal conditions with magnetic field stream lines overlaid and discharge channel outlined.

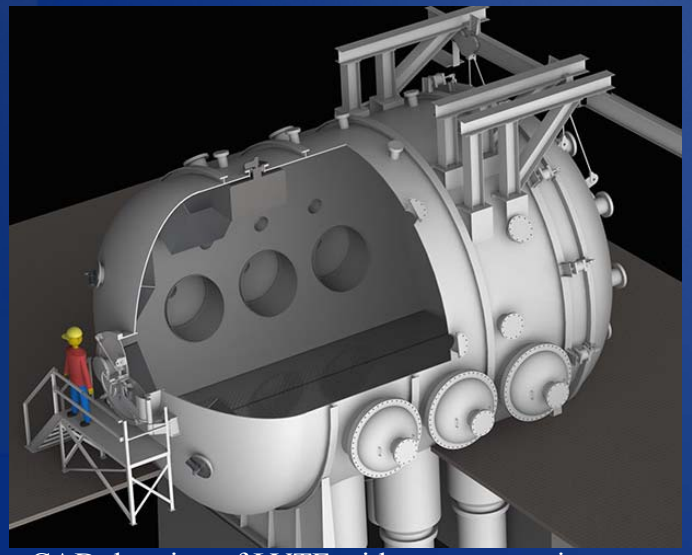

CAD drawing of LVTF with a cutaway view showing the scale.

Configuration

- Internal Cathode
  - Centrally mounted on thruster body centerline.
  - Cathode exit approximately flush with channel exit.
- External Cathode
  - Same cathode, mounted above thruster (12 o'clock position), cathode orifice above edge of outer pole.
  - Cathode exit flush with channel exit.
  - Axially aligned with thruster.
- Probes
  - Moved in front of thruster with radial motion table; not present for all data. Located 120 mm downstream from exit plane.
  - 6 o'clock position (as shown).

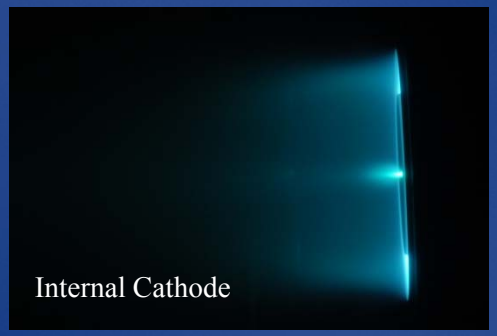
Internal Cathode


External Cathode


Probes

Operating Points

- 300 V/400V/450V, 19.5 mg/s (~20A)
  - Anode 19.5 mg/s, cathode 1.4 mg/s, CFF 7%
  - 9.0e-6 torr corrected for Xe
  - Internal and external cathode
- 300 V, 25.2 mg/s (~28 A)
  - Anode 25.2 mg/s, cathode 1.8 mg/s, CFF 7%
  - 1.2e-5 torr corrected for Xe
- 300 V, 14.7 mg/s (~14 A)
  - Anode 14.7 mg/s, cathode 1.0 mg/s, CFF 7%
  - 6.1e-6 torr corrected for Xe
- Pressure not varied intentionally, set by pumping speed except for extra 300 V cases.

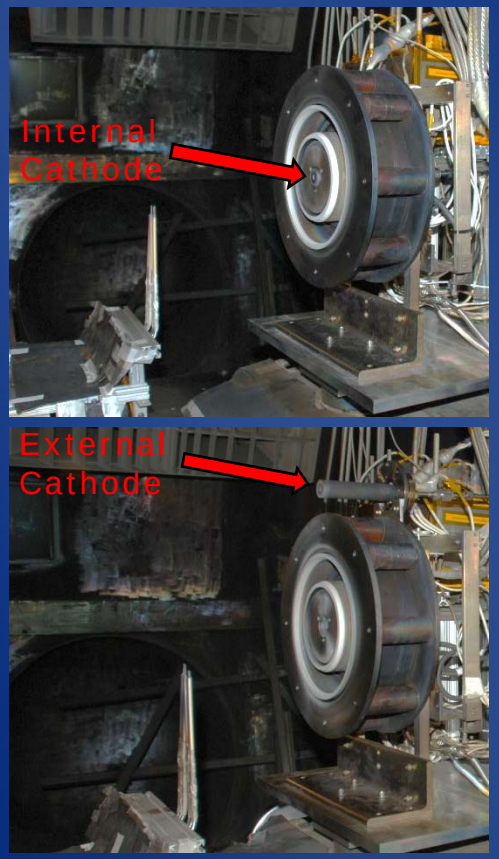

Internal cathode (top) and external cathode (bottom) configurations shown with probes.

	14.7 mg/s	19.5 mg/s	25.2 mg/s
300 V	1	4	1
400 V	0	2	0
450 V	0	1	0

Test matrix showing discharge voltage and anode flow rate variations for the internal cathode configuration. Green: tested, Red: not tested. Number indicates the number of sweeps at the condition.

Mode Transition

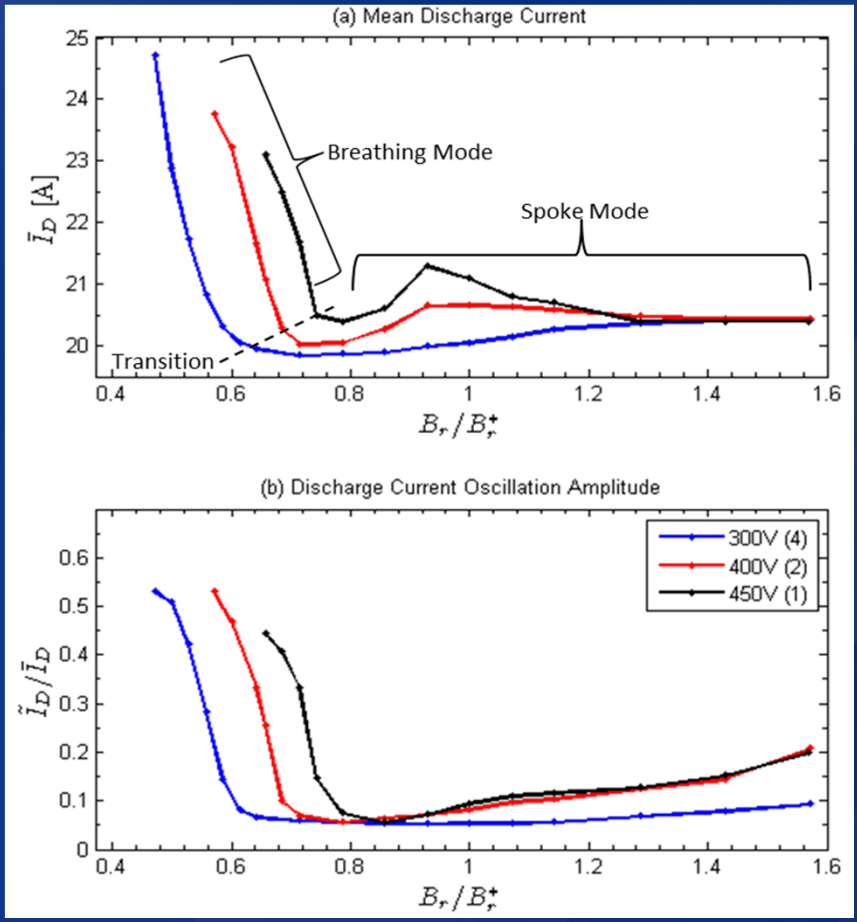

Discharge current mean (a) and oscillation amplitude (b) variation with constant 19.5 mg/s anode flow rate and variable discharge voltages of 300, 400 and 450 V. The number in parenthesis is the number of sweeps averaged together.

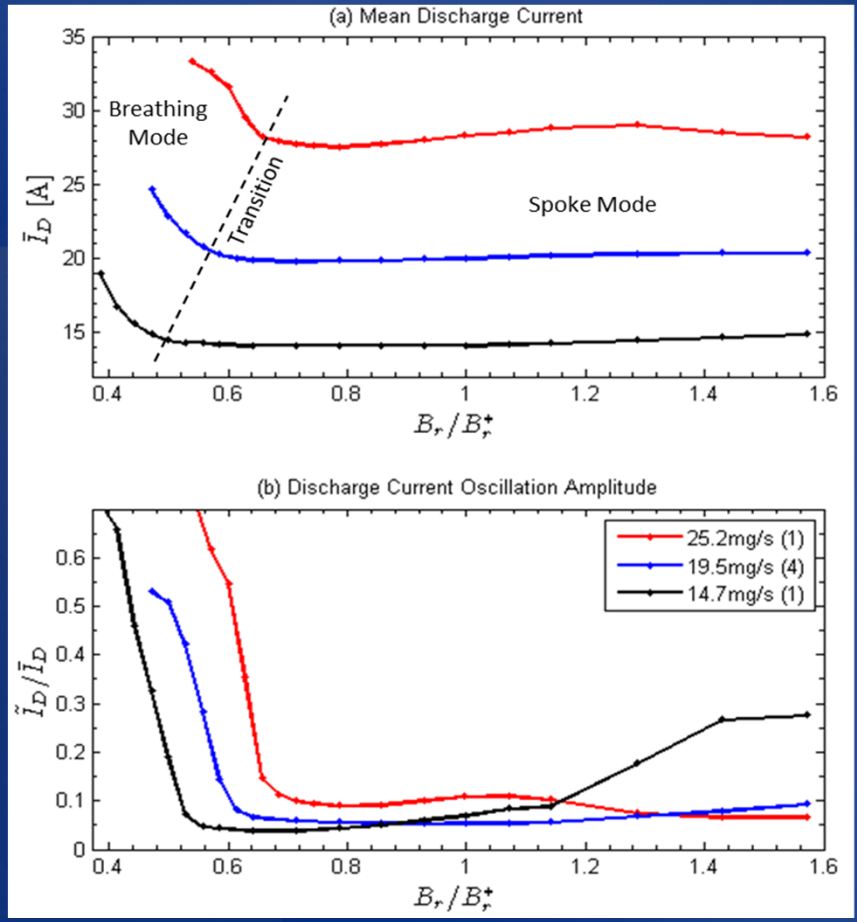

Discharge current mean (a) and oscillation amplitude (b) variation with constant 300 V discharge and variable anode flow rates of 25.2, 19.5 and 14.7 mg/s. The number in parenthesis is the number of sweeps averaged together.

Telemetry Data

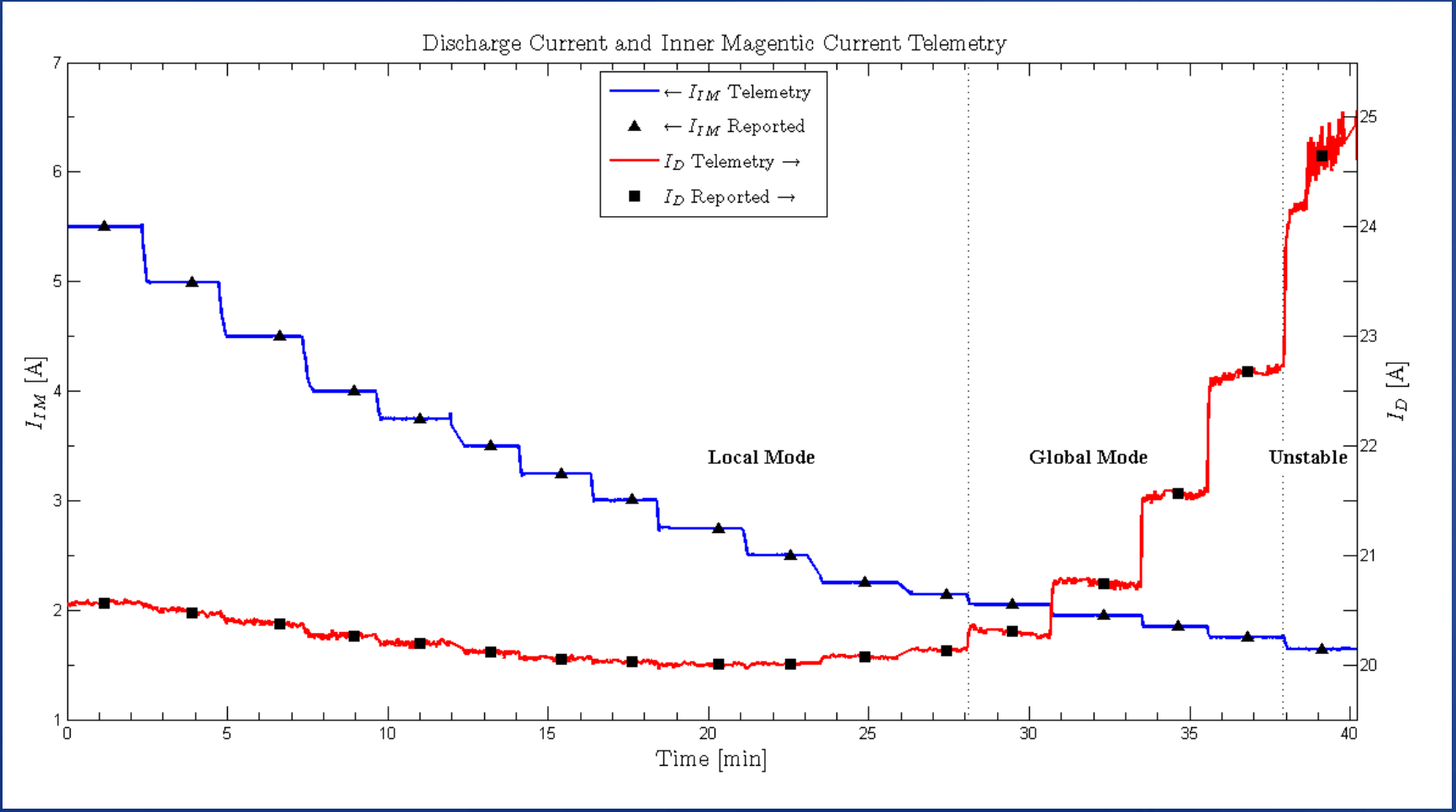

Telemetry for discharge current and inner magnet current for a B-field sweep at 300 V, 19.5 mg/s recorded at 1 Hz. The B_r/B_r^* regions of local mode, global mode and unstable operation are noted.

Mode Transition and HIA

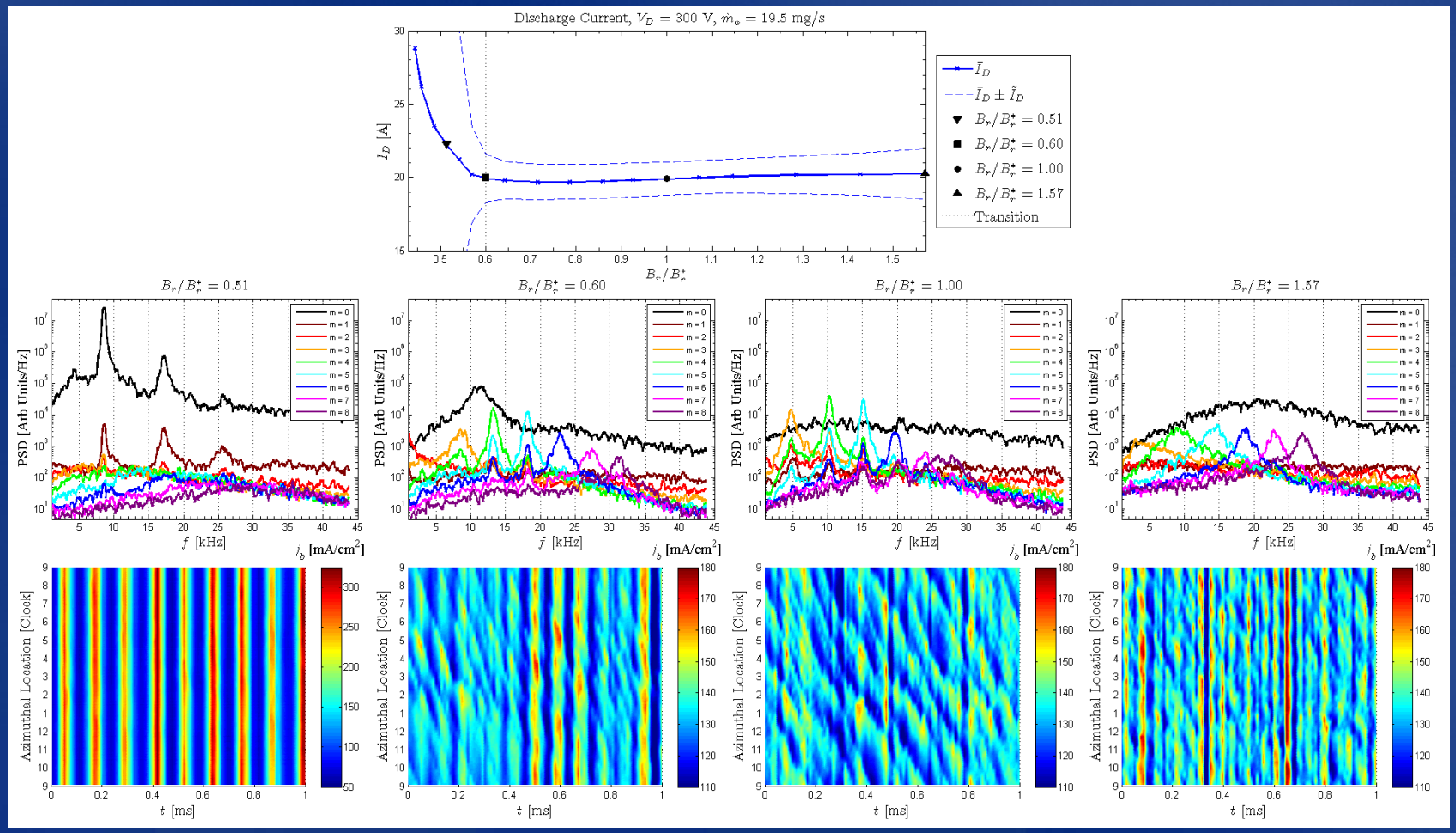

B-field sweep for 300 V, 19.5 mg/s showing transition at B_r/B_r^* = 0.60. The discharge current mean and oscillation amplitude are shown with transition and for B_r/B_r^* settings selected for further analysis. The middle row plots are FastCam PSDs and the bottom row plots are spoke surfaces. The discharge current density scale range for B_r/B_r^* = 0.51 discharge current density surface is larger due to the magnitude of fluctuations. A 500 Hz moving average filter has been applied to smooth all PSDs.

Mode Transition with Probes

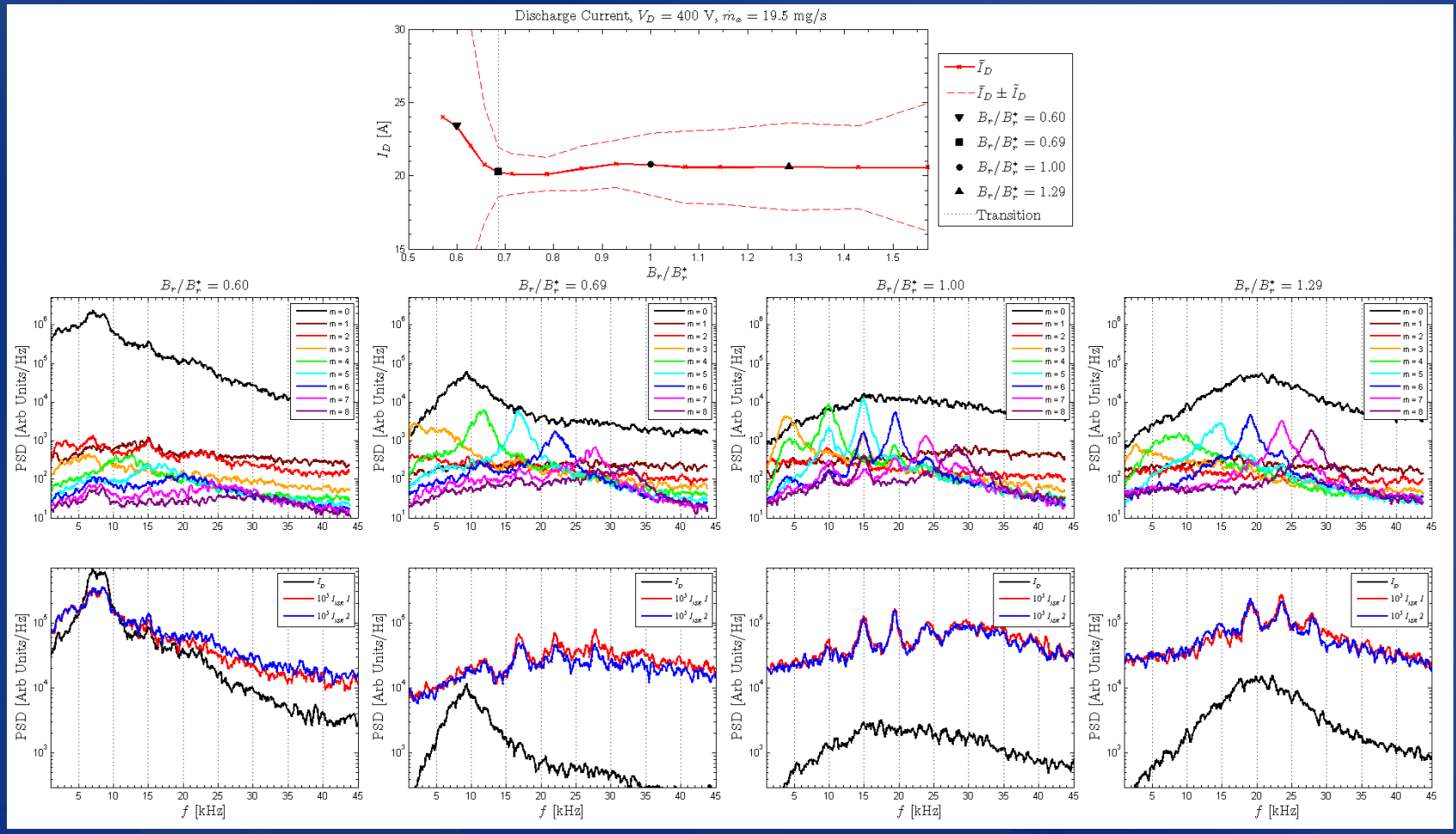

B-field sweep for 400 V, 19.5 mg/s with probes in place showing transition at $B_r/B_r^* = 0.69$. The discharge current mean and oscillation amplitude are shown with the transition and for B_r/B_r^* settings selected for further analysis. The middle row plots are FastCam PSDs and the bottom row plots are discharge current and ISR signal PSDs. A 500 Hz moving average filter has been applied to smooth all PSDs.

Transient Probe Response

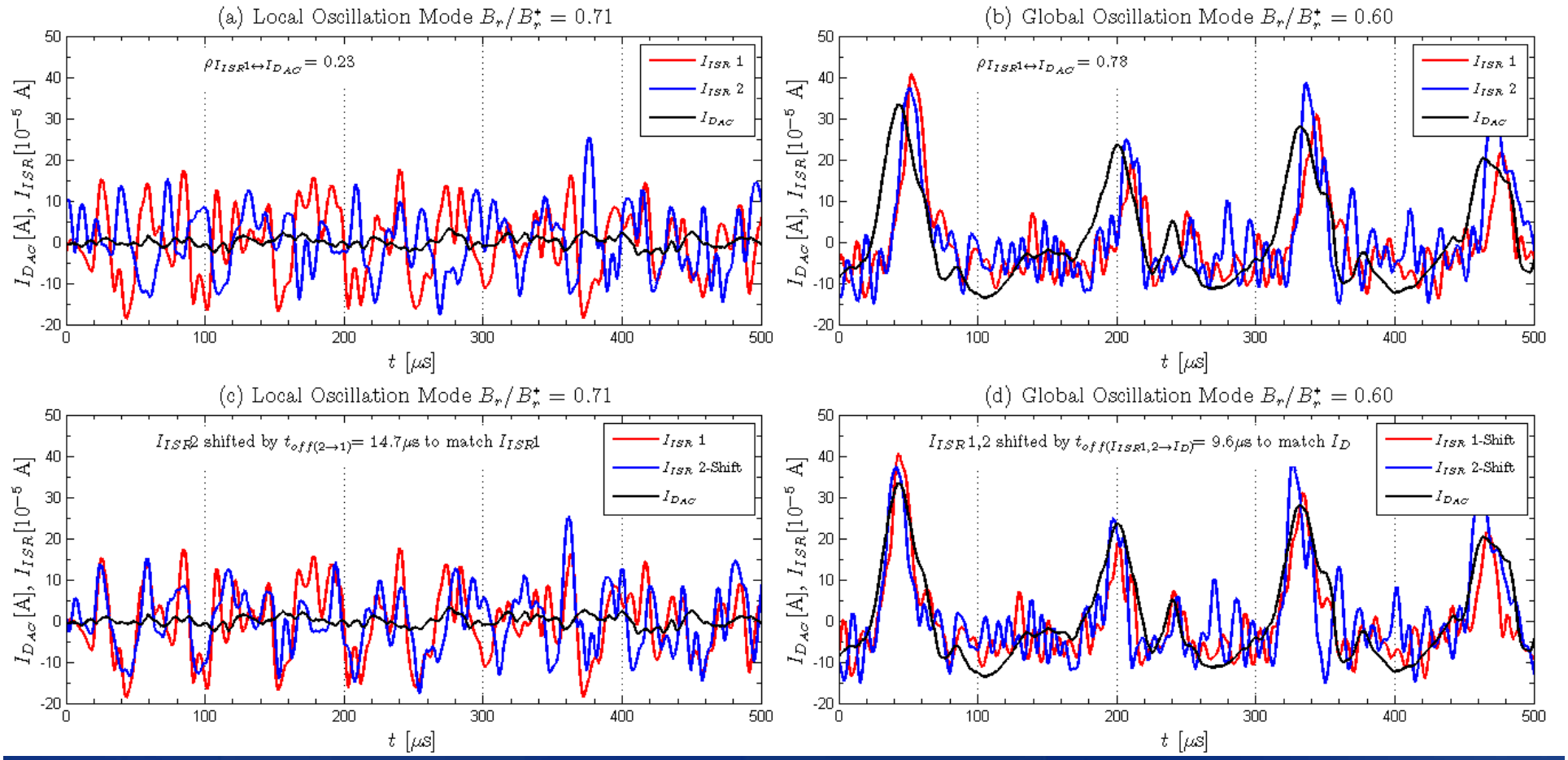

Comparison of AC-coupled discharge current ($I_{D\,AC}$) to AC-coupled ISR current (I_{ISR1} and I_{ISR2}) for 400 V, 19.5 mg/s. Note the I_{ISR} signals have been scaled by 10^5, the I_{DAC} signals are true scale. The ISR signals were low-pass filtered at 150 kHz using a Butterworth 3rd order filter to reduce noise.

Correlation between ISR probes and Discharge Current

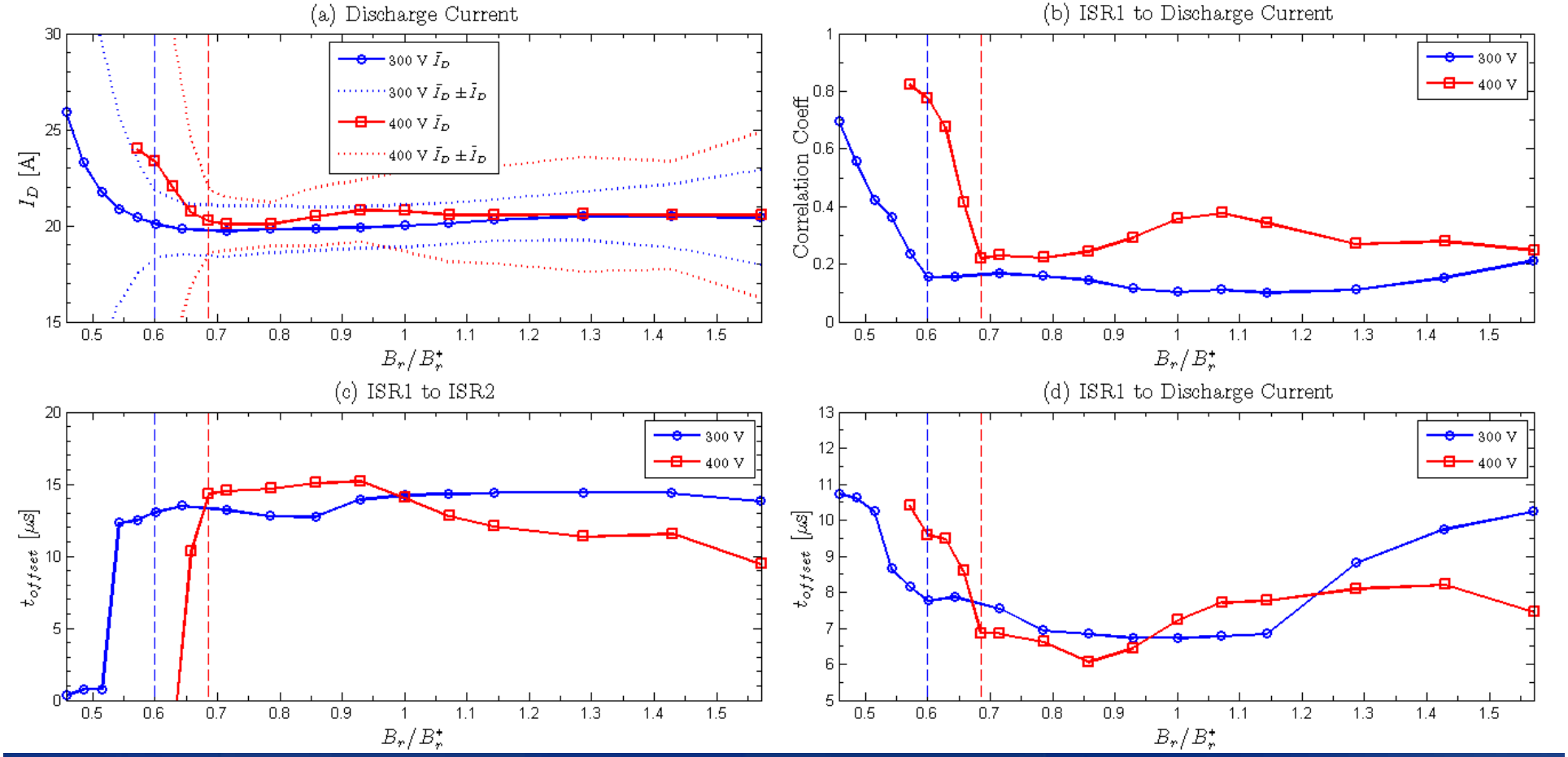

B-field sweeps at 19.5 mg/s for 300V (blue) and 400 V (red) with ISR probes; transition points are shown as vertical dashed lines. (a) Discharge current mean values with oscillation amplitude in dotted lines. (b) Correlation coefficient from ISR1 to discharge current. (c) Time offset from ISR1 to ISR 2 calculated from cross-correlation (d) Time offset from ISR1 to discharge current calculated from cross-correlation.

Thrust and Thrust to Power during Transition

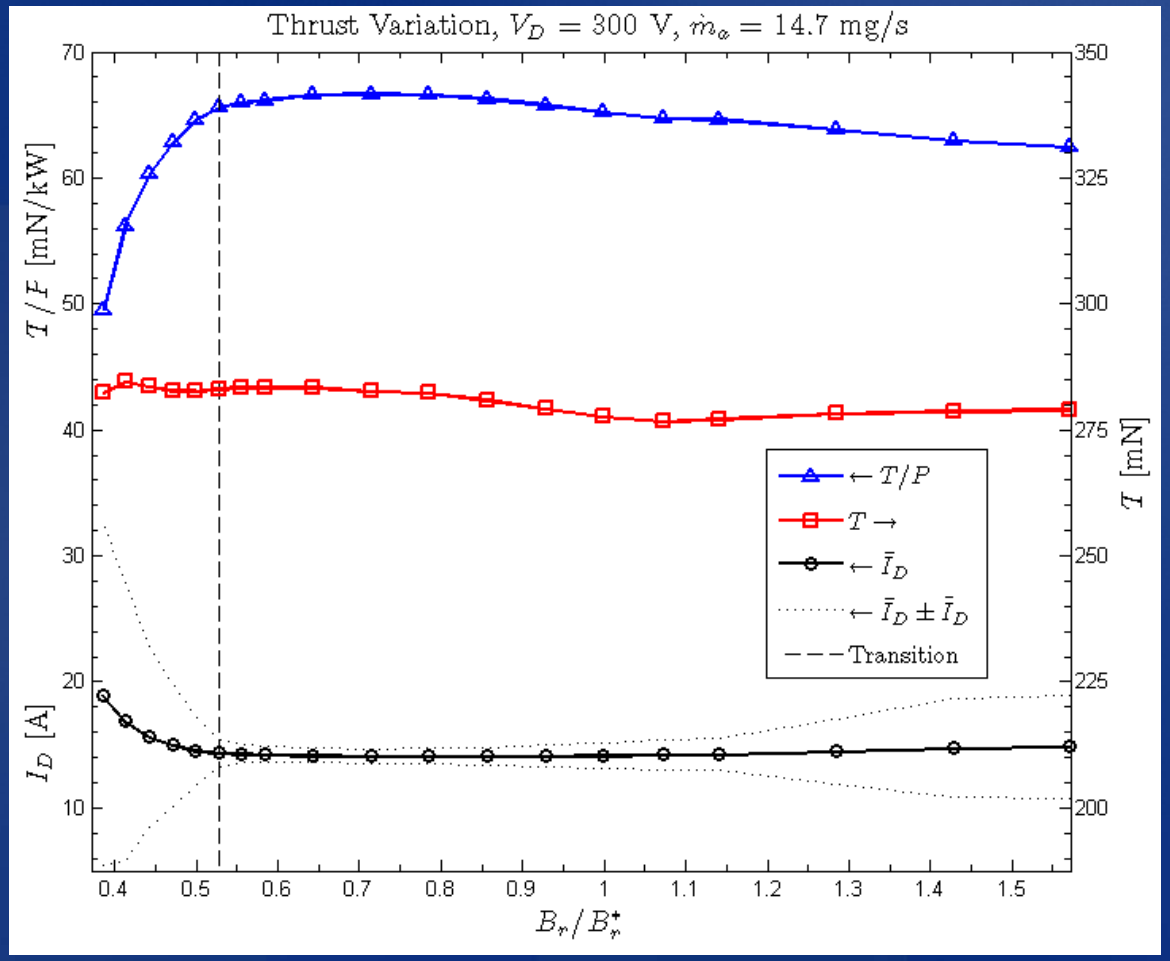

Thrust and T/P for 300 V, 14.7 mg/s during B-field sweep. The thrust is constant at 281 mN within experimental error, but the T/P decreases below the transition point as the discharge current increases.

Mode Transition with Internal Cathode

300 V, 19.5 mg/s, Internal Cathode

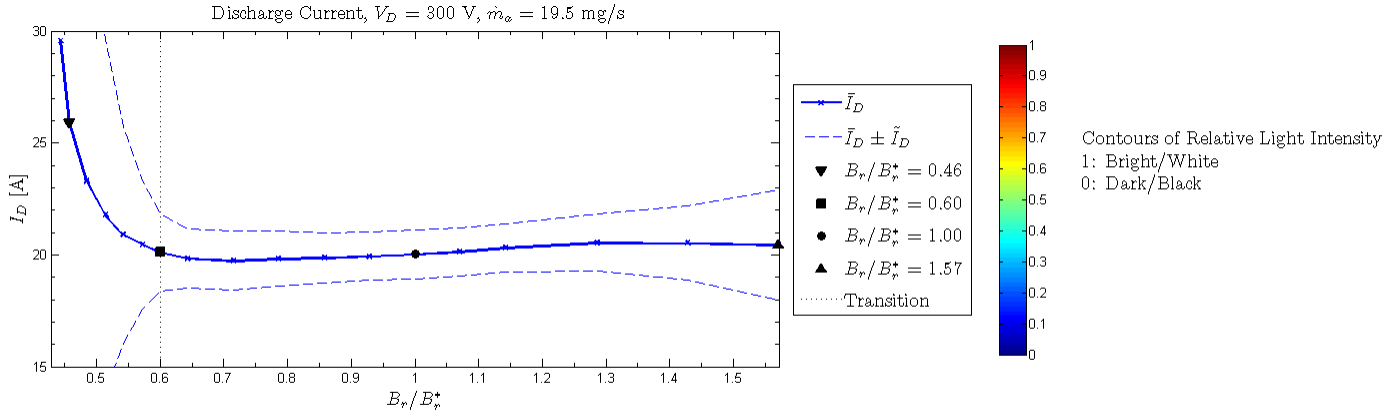

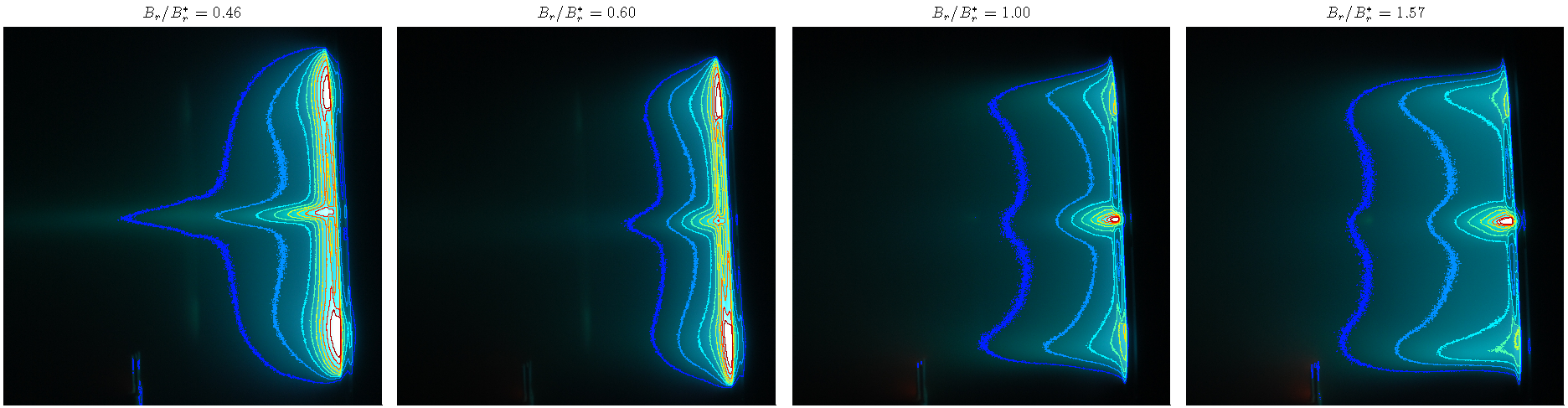

Mode Transition with External Cathode

300 V, 19.5 mg/s, External Cathode

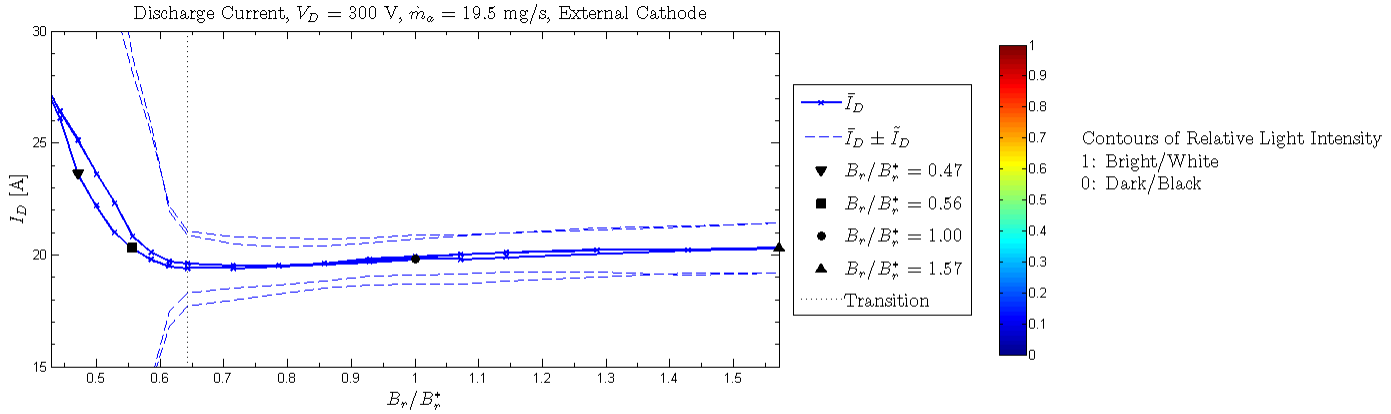

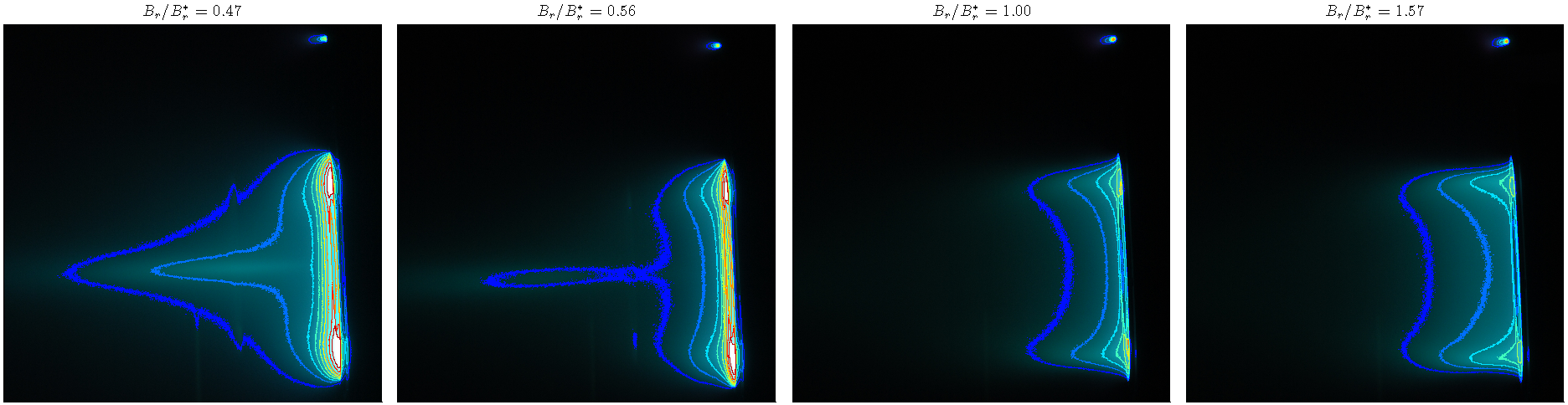

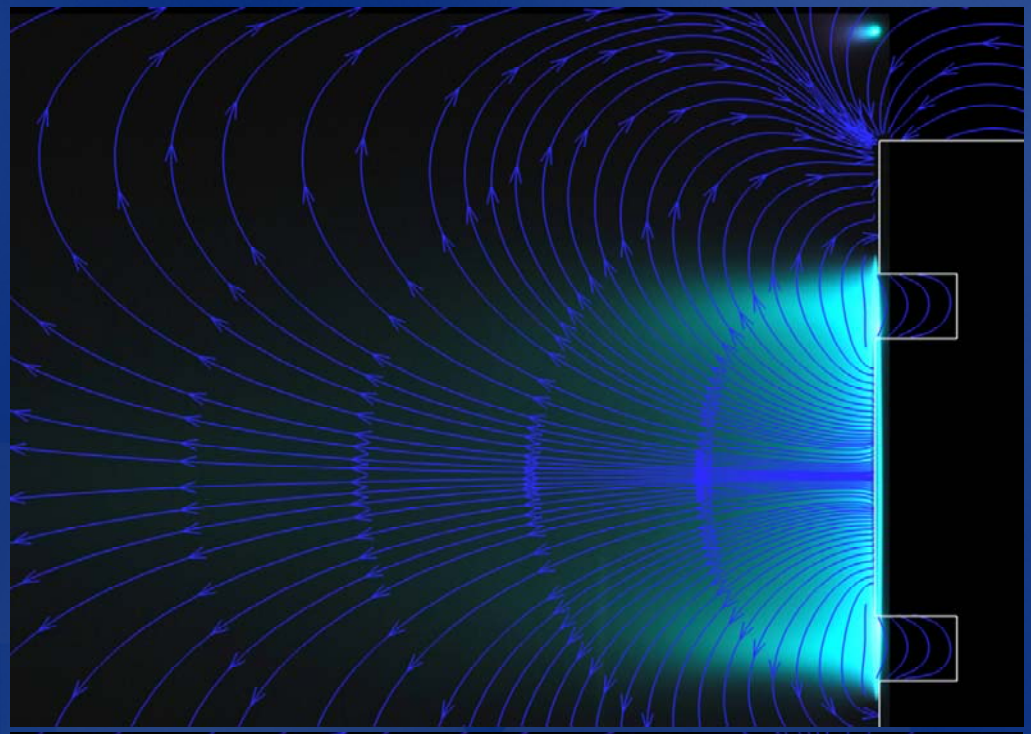

Local Oscillation Mode
$B_r/B_r^* = 1.00$
$V_D = 300$ V
$m_{dot} = 19.5$ mg/s
$I_{D\ mean} = 19.8$ A
$I_{D\ RMS} = 1.09$ A
External Cathode

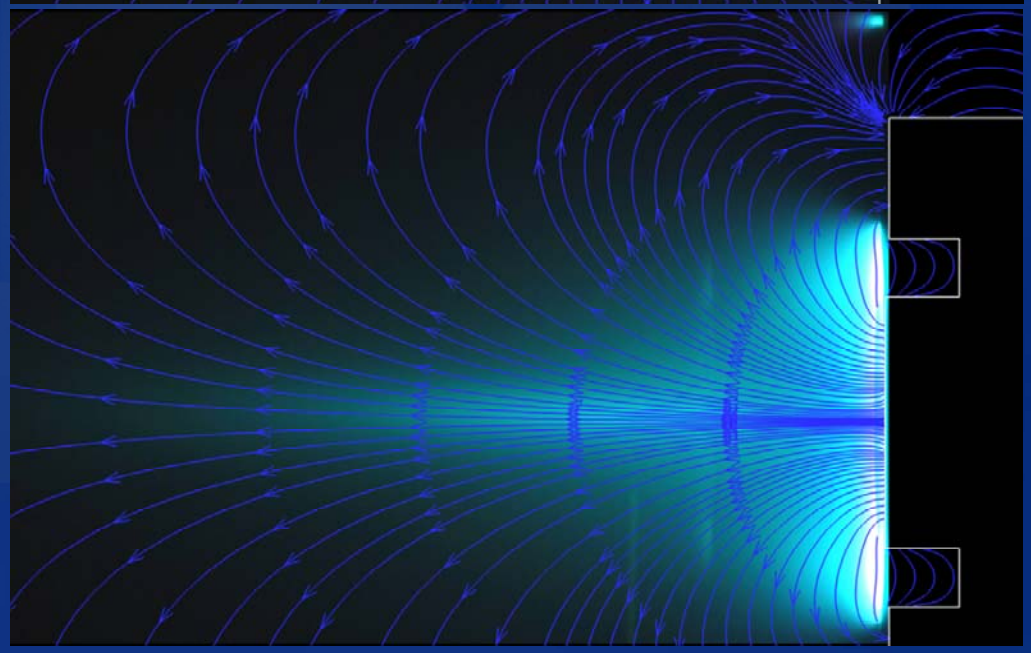

Global Oscillation Mode
$B_r/B_r^* = 0.47$
$V_D = 300$ V
$m_{dot} = 19.5$ mg/s
$I_{D\ mean} = 23.6$ A
$I_{D\ RMS} = 13.6$ A
External Cathode

Definition of Mode Transition

- **Global Oscillation Mode**
  - The discharge current density in the entire channel is oscillating in unison with peak values of order 100% of the mean value and azimuthally propagating perturbations are either entirely absent or of negligible magnitude with respect to the discharge current density peaks. The m_0 mode of the HIA PSD has a clearly defined peak value and spoke orders $m > 1$ do not have peaks more than an order of magnitude above the general noise floor. Azimuthally spaced probes do not observe delays in plasma property oscillations indicative of the entire channel oscillating in unison, and are well correlated to the discharge current with $r > 0.3$. The discharge current oscillation amplitudes (RMS) are well above 10% of the mean discharge current value and the mean discharge current is over 15% higher than the minimum discharge current value obtained in a sweep. The discharge channel and near-field plume regions are observed to be brighter indicative of increased collisions in the plume; a spike of bright plasma is visible on thruster centerline.
- **Local Oscillation Mode**
  - The discharge current density oscillations are dominated by localized perturbations that are less than 25% of the mean value and propagate in the E×B direction. Oscillations may be present where the entire channel increases or decreases in unison, but they are sporadic and do not dominate the azimuthal propagations. The m_0 mode of the HIA PSD has a very broad peak value and spoke orders $m > 1$ have peaks more than an order of magnitude above the general noise floor. Azimuthally spaced probes observe clear delays in plasma property oscillations indicative localized regions of increased ionization within the discharge channel propagating downstream. The probe signals are not well correlated to the discharge current with $r < 0.3$. The discharge current oscillation amplitudes (RMS) are less than approximately 10% of the mean discharge current value and the mean discharge current is within 15% of the minimum discharge current value obtained in a sweep. The discharge channel and near-field plume regions are observed to be dimmer indicative of decreased collisions in the plume and collisional processes more confined to within the discharge channel. The plasma is well focused on discharge channel centerline and the center spike of plasma is absent for an external cathode or greatly diminished for an internal cathode; an internal cathode will always produce a spike on thruster centerline because it is a plasma source.

Conclusions

- Previous researchers have identified mode transitions in HETs where a small change in a thruster operating parameter such as discharge voltage, magnetic field or mass flow rates cause the thruster discharge current mean and oscillation amplitude to increase significantly. Mode transitions in the H6 were induced by varying the magnetic field intensity while holding all other operating parameters constant and measurements were acquired with ion saturation probes and ultra-fast imaging. A technique was developed that calculated discharge current density oscillations from FastCam images of the discharge channel in order to quantify the fluctuations. Spokes are localized oscillations that are typically 10-20% of the mean discharge current density value while the global oscillation mode can be 100% of the mean value.
- The modes are described here as global oscillation mode and local oscillation mode. In global mode the entire discharge channel is oscillating in unison and spokes are either absent or negligible with discharge current oscillation amplitude (RMS) greater than 10% of the mean value. Downstream azimuthally spaced probes show no signal delay between each other and are very well correlated to the discharge current signal. In local oscillation mode perturbations in the discharge current density are seen to propagate in the E×B direction with clear spokes shown in a HIA PSD. The discharge current oscillation amplitude and mean values are significantly lower than global mode. Downstream azimuthally spaced probes show a clear signal delay between each other indicating the passage of spokes but are not well correlated to the discharge current indicating localized plasma oscillations within the discharge channel. The mode transitions were consistent across different tests and showed no hysteresis, but did change at different operating conditions. The transition between global mode and local mode occurred at higher relative B-field strengths for higher mass flow rate or higher discharge voltage.
- The thrust was constant within experimental error through the mode transition but the thrust to power decreased by 25% for the 14.7 mg/s flow rate; the peak in thrust to power occurs near the transition point. The plume showed significant differences between modes with the global mode significantly brighter in the channel and the near-field plasma as well as exhibiting a plasma spike on thruster centerline. For the external cathode case the plasma spike disappeared in local oscillation mode. Based on the research presented here the H6 should be operated in local oscillation mode to minimize discharge current and maximize performance.